FCP Report No. 49

EFFECTS OF FATIGUE IN THE ELASTIC REGIME ON THE MECHANICAL PROPERTIES OF LOW-CARBON STEELS

by

Alexander W. Riedy and James F. Stubbins
Nuclear Engineering Program

Three low-carbon steels, one ferritic (SAE 1018) and two bainitic (A533B Cl I and Cl II) all with similar compositions, were fatigued in the elastic regime at a stress amplitude of 207 MPa to 10^4 and 10^6 cycles at 7.5 Hz at temperatures of 25°C and 300°C (only bainitic steels). Following fatigue, changes in tensile, notch-tensile, micro-hardness, and microstructural properties were determined. The data obtained indicates that elastic fatigue causes SAE 1018 to soften, and increases notch-tensile ductility in all three steels. Transmission electron micrographs show an increase in dislocation density and the generation of subgrains with fatigue at 10^6 cycles and from incremental over-strain tests to 1% strain.

A Report of the

FRACTURE CONTROL PROGRAM

College of Engineering, University of Illinois
Urbana, Illinois 61801

December, 1983

ACKNOWLEDGEMENTS

This investigation was conducted in the Materials Engineering Research Laboratory (MERL) at the University of Illinois, Urbana-Champaign. It was sponsored by the Fracture Control Program, College of Engineering. We are indebted to Peter Kurath, Jay Fash, and Peter Furman for their help. We would also like to thank Dr. D. A. Canonico of Combustion Engineering, Inc. for providing the A533B Class I steel for the experiments. For a superb and timely job in machining test specimens special thanks goes to Paul Douglas of the Theoretic and Applied Mechanics Machine shop. For a fine typing job, warm thanks goes to Marcia Haill of the Nuclear Engineering Program.

TABLE OF CONTENTS

LIST OF TABLES

LIST OF FIGURES

Figure | Page

1.0 INTRODUCTION

Due to the large quantities of steels used in structural and load bearing applications, there is a continuing interest in the fatigue and fracture properties of these important engineering materials. A large body of data has been collected and several theories have been advanced in an attempt to understand and explain failure processes. A particularly worrisome aspect of steel failure is failure by cleavage, or brittle, fracture. The tendency for brittle failure is a sensitive function of material chemistry and microstructure, severe temperature, inclusion content and morphology, heat treatment, and load history.

It is well established that steels exhibit a fatigue (endurance) limit, that is a fatigue stress amplitude below which failure does not occur, even at very large numbers of reversals. This fatigue limit is usually on the order of one third of ultimate tensile strength, but in any case well within the elastic region. Sinclair and others have shown that cycling below the fatigue limit can actual strengthen some steels so that materials subjected to subsequent increases in stress amplitude have longer lives than would be predicted for virgin material. This effect may be due to the development or rearrangement of the steel's microstructure, particularly the dislocations, during elastic cycling. This intriguing process may also yield benefits for other materials properties as a consequence of elastic fatigue. In addition, the extent of the effect should be sensitive to the starting material microstructure. The present study explores this possibility by studying three steels all of nearly the same composition. The heat treatments are different, though, so that the initial microstructures and strengths are different. The structures represented are: a low to medium strength ferritic steel (SAE 1018), a low to medium strength bainitic steel (A533B Class I) and a medium to high strength bainitic steel (A533B Class II). The effects of elastic fatigue cycling on tensile and hardness properties and on microstructure are studied for these steels in the following report.

2.0 LITERATURE SURVEY

2.1 Brittle Fracture Theories

Prior to the early 1970's, two different concepts were used to explain brittle fracture in iron and steel. Early theories of brittle fracture in iron and steel were developed by Griffith,[1] Ludwik,[2] and Orowan.[3] Their theories related cleavage (brittle) fracture to pre-existing cracks. It was proposed that brittle cleavage fracture took place at low temperature, because the normal stress needed to propagate pre-existing cracks was less than the material's yield stress. Eldin and Collins[4] and Wessel[5] ran tensile tests at various temperatures, and their data supported this early theory. They found that the brittle fracture stress values at low temperatures fell below the extrapolated yield stress curve.

One problem with their approach was the size of the crack required for brittle fracture. The critical crack size c can be estimated with the Griffith-Orowan[1] equation:

$$c = \frac{E\gamma}{\sigma_f^2} \qquad [1]$$

where σ_f is the brittle fracture stress, γ is the effective surface energy of the crack, and E is Young's Modulus. When previous estimates such as $\sigma_f = 6.89\times10^2$ MPa (100 ksi), $\gamma = 100 J/m^2$ (6.85 lb/ft), and $E = 2.068\times10^5$ MPa (30,000 ksi) were used in the above equation a critical crack size of $c = 4.0\times10^{-5}$ m (1.3×10^{-4} ft) was obtained. Cracks of that size were within an order of magnitude of the grain size of low carbon steels, but were rarely observed in annealed steel or iron.

A second theory was proposed by Cottrell(6) in 1958. Cottrell stated that brittle fracture in steel, and perhaps most other metals, was started by plastic deformation. He suggested that during the fracture process there were three separate stresses from which different fracture mechanisms could arise: the yield stress, at which existing slip bands would initiate slip in near by bands; the nucleation stress, at which slip bands would nucleate microcracks; and finally the growth stress, at which the microcracks propagate to complete fracture. Cottrell claimed that the nucleation stress was smaller than the growth stress, so the crucial comparison was between the yield and the growth stress. When the yield stress was larger than the growth stress the material was brittle; and when it was smaller the material was ductile. Cottrell(6) offered an additional mechanism to explain brittle fracture: coalescence of two mobile dislocations to form a microcrack on a cleavage plane and eventually a cleavage crack.

Cottrell's theory predicted a ductile-brittle transition and Eq. [2] and [3] defined the transition point: (See Figure 2.1)

$$(\sigma_1 d^{1/2} + K_y)K_y = \beta\mu\gamma \qquad [2]$$

or equivalently,

$$\sigma_y K_y d^{1/2} = \beta\mu\gamma \qquad [3]$$

where $\beta = 1$, μ is the shear modulus, σ_y is the yield stress, γ is the surface energy of the material, and d is the grain diameter. K_y in Eq. [3] is defined as:

$$K_y = \sigma_d \ell^{1/2} \qquad [4]$$

where ℓ is the distance from the piled-up avalanche of dislocations to the nearest sources, σ_d is the unpinning stress for the temperature and time concerned, and σ_1 is the stress resistance met by a released dislocation as it glides along its slip plane.

The left hand side of Eq. [3] represents the energy required for materials yielding, that is, plastic or ductile deformation. The right hand side represents the energy required to form new crack surface area in existing microcracks. When the energy for yielding is greater than that for crack surface formation, cracks will grow and the material will fail by brittle fracture. If the energy required for surface formation is greater than that for yielding, the material will plastically deform and experiences only ductile failure. Thus, Eq. [2] or [3] defines the transition between these two failure modes.

Increases in K_y, σ_1, σ_y, and d, all tend to make the metal brittle. The critical factor is K_y because it determines the number of dislocations released into a slip band when a dislocation source is unpinned.

The effects of grain size and temperature on the yield and facture stresses of low carbon steels can be seen in Figures 2.1 and 2.2 respectively.

In contrast to Griffith's theory, Cotrell's stated that cleavage fracture was induced by deformation not by pre-existing cracks. Cottrell's theory not only predicted a tensile stress-controlled cleavage fracture, but also explained the effects of grain size and yielding parameters on fracture. It did, however, neglect the possible influence of other microstructural variables besides grain size.

Hahn, et al.,(9) investigated the concept of deformation induced fracture, and proposed that pre-yield microstrain was one of the mechanisms of the fracture phenomenon. Hahn and coworkers found that the formation of microcracks and the occurance of cleavage fracture were preceded by plasitic deformation. Their results supported the concept that cracks responsible for cleavage fracture were not present initially, but were generated by the deformation process. Their results showed a temperature dependence of yield an fracture stress similar to that found by Parker (See Figure 2.2). They concluded that the initiation of cleavage within a grain, that is, the formation of a microcrack, was not the only criterion needed to propagate a crack to fracture. Hahn further stated that yielding at low temperature was governed by slip or twinning, which inturn controlled fracture, while at high temperatures yielding was governed by mechanisms that led to propagation of new microcracks. He also suggested that the Griffith-Orowan equation could describe the conditions for propagating microcracks.

The influence of other microstructural parameters on fracture was clearly shown in work by McMahon and Cohen[10] in low temperature tensile tests on ferritic steels with similar flow and yield properties, but different carbide particle distributions. They found that over 90% of the cleavage cracks were initiated by cracking of iron-carbide particles (cementite: Fe_3C) even when the metal's carbon content was as low as 0.007%. They proposed the following explanation for the generation of a cleavage microcrack in ferrite: a crack initiates in a cementite particle after plastic deformation in neighboring ferrite. It propagates across the brittle carbide as a Griffith flaw. At sufficiently low temperatures, this cracking could initiate cleavage microcracks in surrounding ferrite. But when slip or twinning occured in ferrite no microcracks would appear. In their experiments McMahon and Cohen found that the probability of microcrack formation (cleavage cracks in the ferrite grains) increased with increasing carbide particle size and with decreased test temperatures. They also found that a majority of the microcracks in ferrite were produced in the strain hardening stage of the stress-strain curve, when carbide cracks were forming. Lindley, Oates, & Richards'[11] investigations of low-carbon iron led to the conclusion that both microscopic (dislocation pile-ups) and macroscopic (fiber loading) mechanisms were needed to model the cracking behavior of cementite particles. The fiber mechanism is a method of calculating the stresses in cementite films induced by stresses applied to ferrite grains. They calculated that the maximum tensile stress was at the center of carbide films at grain boundaries along the direction of loading, and thus predicted carbides oriented along the tensile axis to crack most readily. They concluded that carbide cracks could be generated by slip and twinning in the pre-yield microstrain region at low temperatures, but at higher strains, ferrite cracking was controlled by the fiber loading concept.

Additional studies on cleavage fracture were undertaken by Man, Vlach, & Holzmann[12] on coarse and fine grained low-carbon steels. They examined the effects of grain size, grain-boundary cementite thickness, and pearlite on fracture behavior at a range of temperatures. They found that the ductile brittle transition region was related to grain size and cementite thickness. The temperature region of semi- brittle fracture was expanded with increasing cementite thickness. They also found no influence of pearlitc phases (ferrite and cementite) on embrittlement. They concluded that two stresses were necessary to explain cleavage fracture: the stress required for propagation of microcracks through grain boundaries and the stress required for microcrack growth into ferritic grains.

More recent investigations by Richie, Knott, and Rice[13] and Richie, Server, and Wullaert[14] have dealt with fracture stress and fracture toughness of high-nitrogen mild steels and two pressure vessel steels, A533B Class I and A302B. Richie, Knott, and Rice developed a mathematical model to predict the variation of fracture toughness (K_{IC}), over a temperature range of -150°C (-238°F) to -75°C (-103°F), knowing the yield stress and hardening properties. This variation was established by previous experiments. They determined that fibrous fracture initiated ahead of the notch tip, by calculating the location of the maximum achievable stress intensification. They also developed a relationship between the model for fracture ahead of a rounded notch, and that ahead of a sharp crack. Richie, Server, and Wullaert used simple fracture models to predict the temperature variation of plane strain fracture toughness in unirradiated and irradiation nuclear pressure vessel steel. Their models combined continuum mechanics solutions for strain and stress distributions ahead of crack tips with simplified theories of the microscopic fracture mechanisms involved. The Richie-Knott-Rice model regarded the cleavage fracture stress as a general material property and did not deal with the statistical nature of cleavage crack nucleation.

Curry and Knott(15-21) have jointly and individually authored several papers on the effects of microstructure on fracture toughness and cleavage fracture stress in ferritic steels. Their model attempts to quantitatively analyze the cleavage fracture toughness of quenched and tempered steels. They assumed the crack nucleus size distribution can be represented as some multiple of the carbide particles size distribution. The probability of finding a crack nucleus subjected to a stress equal to or greater than the appropriate local fracture stress was estimated for each crack nucleus radius. This was summed over all crack nucleus radii and cleavage theoretically occured when the probability term was equal to unity. With their model, it was possible to predict the fracture toughness of a steel from its carbide particle distribution.

It has been shown by several researchers that σ_f is strongly dependent on grain size, being higher for fine grained materials (see Figure 2.3). Curry and Knott determined a relation between the largest observed carbide thickness and ferrite grain size in annealed and normalized mild steels. If it was assumed that the largest observed carbide particles gave rise to fracture, this fact could be used in conjunction with Eq. [5] to predict the grain size dependence of the cleavage fracture stress. This equation is given as,

$$\left(\frac{C_o}{d}\right) \sigma_f^2 + \tau_e^2 \left\{1 + \frac{4}{\pi} \left(\frac{C_o}{d}\right)^{1/2} \frac{\tau_i}{\tau_e}\right\}^2 \geq \frac{4E\,\gamma_p}{\pi(1-\nu^2)d} \qquad [5]$$

where C_o is the thickness of the grain boundary carbide, E is Young's modulus, γ_p is the effective surface energy of ferrite, d is the slip band half-length, ν is Poisson's ratio, τ_i is the lattice friction shear stress, σ_f is the fracture stress, and τ_e is the effective shear stress. The right hand side of Eq. [5] is equivalent to the Griffith equation. Curry and Knott[19] assume that if the effective shear stress τ_e is written as $K_y d^{-1/2}$ where d is now the grain size, the fracture criterion (Eq. [5]) reduces to:

$$\sigma_f^{\,2} + \frac{(K_y^s)^2}{C_0}\left\{1 + \frac{4}{\pi}(C_0)^{1/2}\frac{\tau_i}{K_y^s}\right\}^2 \geq \frac{4E\,\gamma_p}{\pi(1-\nu^2)C_o} \qquad [6]$$

This predicts that the only microstructural parameter affecting the fracture stress is the carbide thickness, since K_y is a measure of the ease of unpinning or creating dislocations and is independent of grain size. Predictions made using Curry and Knott's model were seen to be in good agreement with experimental results for a variety of temperatures and steels.

Although the Richie-Knott-Rice model neglected the statistical nature of cleavage, it nevertheless yielded essentially identical predictions to those of the statistically based Curry and Knott model, and provides a wholey adequate description of the process of cleavage fracture in steels. Both of these models are valid only over the temperature range where metals show brittle behavior. The Curry and Knott and the Richie-Knott-Rice models are the most comprehensive fracture theories to date.

2.2 Effects of Fatigue on Microstructure and Mechanical Properties

There have been numerous research efforts on fatigue damage and dynamic strain aging of low-carbon steel. Some early research on the effect of fatigue on cold-worked metals was done by Polakowski and Palchoudhuri.[22] They stated that past results have shown that initially soft metals, that is, hot-worked or annealed metals, were found to harden slightly under the action of alternating stress cycles; their initially low elastic limits, yield points, indentation hardness numbers, and, to a lesser extent ultimate tensile strength values were increased when compared with the unstrained condition. But carbon steels with well developed discontinuous yielding represented an exception to this rule: their yield points were depressed by fatigue stressing in spite of the fact that their matrices hardened. The work of Polakowski and Palchoudhuri was an investigation of the effect of fatigue loads upon the static mechanical properties of several metals (copper, nickel, aluminum, three of their alloys, and a nonaging titanium-killed steel) in the cold worked condition. To avoid the influence of incipient cracks from fatigue, they chose to the use of compression and hardness tests instead of the standard tension test. They postulated that stress cycles of a given type and amplitude should produce a specific condition irrespective of the initial work-hardened condition of the metal being fatigued. Therefore with fixed fatigue cycle parameters, an initially soft material will gradually work-harden until a final hardness level is attained. However, they found that if the same material was initially cold worked by some static method to a hardness level higher that the preceeding maximum, then the same cyclic stress resulted in a softening to a equilibrium level.

Their results indicated that as long as the cyclic stress amplitude during fatigue was substantially lower than the yield point there were only small structural changes in the cold worked metal, and the degree softening was very small, if detectable at all. If the cyclic stress amplitude was increased to levels close to the yield point, plastic deformation occured and the rate of softening increased. Polakowski and Palchoudhuri also discovered that at these higher stress levels the suppression of the yield point became more obvious.

A more indepth study of this effect, including examinations of microstructural changes, was made by Abdel-Raouf and Plumtree[23]. They determined the necessary prior strain conditions whereby no change in the mechanical properties of iron occured during sinusoidal strain controlled cycling. They found that these conditions could be obtained by a critical quantity of prestrain that produced an equilibrium dislocation density and cell size, which corresponded to the expected saturation stress. The annealed iron demonstrated cyclic strain hardening during cycling. The hardening rate decreased with cycles until saturation was attained. Under these conditions, the related substructure showed no marked changes and the stress amplitude became constant. Further cycling at this level in the plastic regime for both annealed and cold-worked metals revealed that the saturation state was independent of the previous strain history of the material and the average cell size remained constant at approximately 1.5 μm.

Sinclair[24] investigated the coaxing effect in fatigue of metals. He found that the fatigue resistance of some metals could be enhanced by cycling below the fatigue limit followed by a process of gradually increasing the amplitude of the alternating stress in small increments, a procedure called coaxing. Experiments have shown that the fatigue limit of some metals could be increased by more than 25% by repeated stressing at or below the fatigue limit of virgin metal.

Sinclair expanded on the earlier studies of Krommers(25), who reported an increase in endurance life of the order of 23,000% for ingot iron, which was cycled below the fatigue limit and coaxed. Sinclair concluded that the coaxing effect in fatigue was governed by a time-dependent localized strengthening through strain aging and not by the ability of the metal to be strengthened by cold work. Present work indicates that strain aging does not result in actual strengthening, but aids in maintaining the materials original strength during plastic deformation.

Mintz and Wilson(26) also used a coaxing procedure and studied the effects cyclic stress on the strain aging phenomenon in various carbon steels. These steels were initially furnace cooled or water quenched and then prestrained to 5% before being fatigued. Disolocation locking was eliminated by the initial prestrain. The change in the temperature of the specimen test section was monitored as criterion for strain aging during cyclic deformation. Energy dissipation concentrated at active slip bands and Mintz and Wilson concluded that aging took place only in these locations. At these areas with relatively higher energy dissipation rates, the activation energy necessary for the formation of precipitates is lowered, leading to strain aging. They also concluded that localized heating during cyclic fatigue was of insufficient duration and magnitude to account for the observed degree of aging.

Wilson and Tromans(27) used optical and electron microscopy in an investigation of the effects of test temperature (20-130°C) and dissolved carbon on the development of fatigue damage in a low-carbon steel. Strain aging during fatigue increased the tendency for cyclic plastic strains to concentrate in active slip bands. At the surface of specimens quenched from 710°C and fatigued above 60°C, damage and continuous slip activity leading to the initiation of cracks was confined within narrow active bands. Beneath the surface, the active slip bands formed parallel channels in fatigue hardened grains. These channels had very low dislocation densities and accommodated large amplitude reversible dislocation movements. In quenched specimens fatigued at 60°C or higher temperatures, evidence of carbide precipitates was seen on dislocations in the clouds and at the edges of active slip bands. This was consistent with the thought that many of the low amplitude dislocations were captured and locked by solute segregation after sufficient amounts of fatigue aging. In this manner, strain aging was believed to have strengthened the fatigue hardened matrix between the active bands and to have created strain concentration within the bands. There was no evidence that the active bands were themselves effectively strengthened by strain aging.

Li and Leslie[28] examined the effects of dynamic strain aging on the subsequent room temperature properties of several carbon steels. The steels were dynamically strained aged with 3 to 9 % strain at various strain rates in the temperature range from 100 to 600°C. Following aging, changes in tensile properties, fatigue life, notch impact transition temperature, and Bauschinger effect* were determined. The effects of aging on the subsequent ambient temperature properties of

---

*Bauschinger effect[29] - phenomena in which applying a stress on a metal in one direction (i.e. compression or tension) until plastic deformation occurs, and which reduces the magnitude of the stress required to produce plastic deformation in the opposite direction. It occurs due to locking of dislocations at obstacles and the development of backstresses.

carbon steels were increases in strength, yield strength-tensile strength ratio, fatigue life, and ductile/brittle transition temperature and decreases in ductility, notch impact toughness, and the Bauschinger effect. Strengthening of the steels came primarily from an enhanced work-hardening rate (enhanced dislocation storage and interaction) during elevated temperature pre-straining.

The effects of strain rate and temperature on the tensile properties of a low carbon nuclear pressure vessel steel were studied by Steichen and Williams.[30] The effect of strain rate on the tensile properties of A533-B steel at temperatures of -157, 22, and 260°C (-250, 72, and 500°F) is illustrated in Figure 2.4. For the test temperature of -157°C (-250°F) they found the yield strength significantly increased with increased strain rate. But, at room temperature and 260°C (500°F) the material was much less rate sensitive and the strength increased only slightly throughout the range of strain rates examined. These results can be seen in Figure 2.4.

Holden[31] investigated the effects of cyclic stressing at the fatigue limit on the subsequent mechanical and metallurgical properties of mild steel. He found that cyclic stressing in increasing step increments, but at or below the fatigue limit (i.e. coaxing) resulted in work hardening and elimination of discontinuous yielding on subsequent monotonic tensile tests. The suppression of the yield phenomenon in the fatigue hardened materials was linked to a decrease in the effectiveness with which dislocations arriving at the boundary of a plasticly deforming grain can activate sources in surrounding grains. The hardening produced by cyclic stressing did not have the temperature characteristics which could be explained by the presence of precipitates on the slip planes that were active during cyclic stressing.

Klesnil and Lukas[32] also studies the effects of cyclic deformation of low-carbon steel at stress amplitudes lower than the macroscopic yield point. They found that at the beginning of the fatigue process microscopic softening occured. This was followed by hardening later in the fatigue life. The initial softening was caused by the expansion of plastically deformed zones where large amounts of free dislocations were active. Microscopic hardening of elementary volumes slowed down the softening process until the entire volume was deformed, and this led to macroscopic hardening. They also derived a model from these studies enabling them to anticipate the quantity of Luders strain that would occur upon further monotonic stressing.

Abel and Muir[33] expanded upon research by Klesnil and Lukas. They ran experiments to determine the differences between the yielding behavior after unidirectional cycling and that following fully reversed (i.e. tension-compression) cycling. They found that cyclic stressing to 2,500 cycles in compression or tension alone would not eliminate the discontinuous yielding phenomenon in subsequent tensile tests, unless the stress amplitude was close to the lower yield stress. But when cycled in the combined tension-compression mode, discontinuous yielding was eliminated with stress amplitudes well below the yield stress.

The discontinuous yielding phenomenon has usually been explained either by the effects linked with the unlocking of dislocations, as in the "static" theories of Cottrell and Bilby[34] and Cottrell, [35,36] or by dislocation multiplication effects as in the "dynamical" theories of Johnson and Gilman[37]. Johnson and Gilman postulated that the strain response of the specimen was a function of the initial mobile dislocation density, velocity, and capacity to multiply. Hahn[38] stated there were three major factors that lead to discontinuous yielding: 1.) a small initial quantity of mobile dislocations, 2.) rapid dislocation multiplication, and 3.) a highly stress dependent multiplication mechanism. Abel and Muir[39] attributed the increased sensitivity of discontinuous yielding from tension-compressing loading to the Bauschinger effect.

In futher studies of this effect, Abel and Muir concentrated on the Bauschinger effect or phenomenon. Their initial aim was to determine which mechanism was responsible for the Bauschinger effect: the back stress mechanism as defined by Mader, et al. [40] or Orowan's[41] mechanism on the directional characteristics of dislocation movement resistance in strained material. They concluded that the major cause of the Bauschinger effect was due to the generation of mobile dislocations in strained material, which showed a directional resistance to additional movement.

In the preceding, several studies of the role of microstructure in the fatigue and fracture were reviewed. To date, no comprehensive theory, precisely relating microstructural quantities and fatigue or fracture behavior, has been evolved. Indeed, for each observed phenomenon, several mechanisms, all seemingly credible, are usually available. It is the goal of the research described in the following to help to clarify certain of these issues.

2.3 Relation to Present Research

The purpose of the present work is to investigate the effects of fatigue (cyclic loading) in the elastic regime on the mechanical and microstructural properties of low carbon steels. The low carbon steels chosen for these experiments were A533B Class I and II, nuclear pressure vessel steels, and SAE 1018, a plain carbon steel used in heavy industry. Both types of steel have a carbon content of about .19 weight % and are similar in manganese, phosphorus, and sulfur content. The A533B steels are of great interest to specialists in the nuclear industry. They are manufactured to have medium to high strength and high toughness values required for present day nuclear pressure vessels. SAE 1018 was picked as a base for comparison with the A533B steel since a great deal of information is known about it. Also the grain size of SAE 1018 is much larger than A533B and this makes microstructural analysis an easier task.

The microstructure of SAE 1018 consists of ferrite and pearlite (ferrite and Fe_3C). The microstructure of A533B is primarily acicular tempered upper bainite with small volume fractions of proeutectoid ferrite, and martensite.(14) It is not possible from optical microscopy to make a clear distinction, but certain studies of A533B Class I claim that the blocky ferrite areas are actually granular bainite since they contain evidence of carbide precipitation. It is anticipated that the steels to be investigated here will show dissimilar results when subjected to fatigue and subsequent mechanical properties testing and microstructural examination. This is expected because of the differences in grain sizes, carbide distributions, and types of phases present in each steel.

3.0 EXPERIMENTAL PROCEDURE

3.1 Materials

The materials used in this investigation were SAE 1018 (a plain low carbon steel), A533B Class I and A533B Class II, (low carbon alloy nuclear pressure vessel steels). The chemical composition of each of these steels is shown in Table 3.2. The SAE 1018 and A533B Class II steels were purchased as 1" thick plates. The A533B Class I* steel was cut from a newly manufactured nuclear pressure vessel, which had undergone a post-weld stress relief heat treatment. All fatigue specimens were cut from the 1/4 plate thickness parallel to the rolling direction. A common fatigue specimen was used for all of the initial mechanical tests on the above steels. (See Figure 3.2)

3.2 Mechanical Testing Techniques

Two different MTS hydraulic test machines, with reversible load designs and maximum loading capacities of 8.9×10^4 N (2.0×10^4 lb.) were utilized in this investigation. For high temperature fatigue and tensile tests, a MTS machine equipped with a high temperature resistance furnace (capable of producing 1000°C) and threaded/hydraulic grips was used. For room temperature fatigue, tensile, and notch-tensile tests, a MTS machine equipped with liquid/solid Woods metal grips was used. Both of these gripping systems ensured uniaxial loading during fatigue cycling or during tensile tests. A flow diagram of the experimental approach can be seen in Figure 3.1. All fatigue, tensile, and notch-tensile tests were controlled

---

*This steel was donated by Combustion Engineering, Inc.

by a PDP-11 mini-computer, and data taken during testing was stored on a floppy disc for later plotting and data reduction of results.

For the high temperature fatigue tests and tensile tests, the temperature was held at a constant 300° ± 2°C. Also, to limit the amount of noise in the exstensometer strain signals, tests were run in the load controlled mode with the use of the "STRESS.BAR" program, my modified version of the constant load amplitude program BILAMP.BØØ. See Appendix A for listing of this program.

Three specimens (see Figure 3.2) were run at each fatigue level for subsequent tensile tests, notch-tensile tests, and microscopic investigation. Fatigue specimens to be used for further tensile tests were axially polished to remove approximately 0.005 in. (.127 mm) from the gauge diameter to eliminate any possibly existing surface cracks. Fatigue specimens used for subsequent notch-tensile tests were machined to specifications as seen in Figure 3.3.

The fatigue tests were run in the fully reversed (sine function) load-controlled mode. The strain amplitudes were monitored with room temperature and high temperature 1 inch MTS exstensometers. Specimens were cycled to 10^4 and to 10^6 cycles at a stress amplitude of ± 30 ksi (207 MPa) approximately 0.1% strain with a zero mean stress, and a frequency of 7.5 Hz. All tests on SAE 1018 were performed at room temperature. Fatigue tests on both classes of A533B were performed at room temperature and at 300°C (572°F).

Tensile and notch-tensile tests were run on as-received and pre-fatigued specimens using the MONOT3.BØØ program. From 0 to 10% strain the tests were strain controlled. Greater than 10% strain the tests were controlled by monitoring stroke (or displacement). A strain rate of 0.0005 sec^{-1} was used for all tests. Tensile tests on the A533B steels were performed at room temperature and at 300°C. Tensile tests on SAE 1018 were all at room temperature. All notch-tensile tests were run at room temperature. Similar notch-tensile tests on aluminum were performed by Kaufman(42) to determine a correlation with fracture toughness.

Impact tests were performed on all the steels in the as-received condition to find the relative toughness of each and to determine the ductille-brittle transition temperature. These tests were run on standard size charpy blocks (see Figure 3.4), at a temperature range of -196°C to 100°C.

Incremental over-strain tests (IOVST) were utilized to determine the cyclic stress strain curve of the as-received steels. The IOVST.BØØ program was used for control of these tests. See Table 3.2 for specifics on experimental procedure.

The following BASIC computer program were utilized in this research and are available on hard disc storage on the PDP-11 minicomputer in the Materials Engineering Research Laboratory (MERL):

STRESS.BAR	- for Load Controlled Tests
BILMMX.BØØ BILHLP.BØØ	for data reduction and plotting of stored data from STRESS.BAR
MONOT3.BØØ	- for Tensile and Notch-Tensile tests
IOVST.BØØ	- for Incremental over-strain tests
BIGIO.BØØ PRNTIO.BØØ	for data reduction and plotting of stored data from IOVST.BØØ

Table 3.3 shows all tests run on the SAE 1018 and A533B steels.

Rockwell hardness tests were performed on the surface of cross-sectioned as-received specimens to find the relative hardness of each steel. A more detailed examination of hardness was made on as-received and fatigued specimens with a Tukon microhardness tester. The purpose of this was to see if fatigue caused an increase in hardness and to see if this hardness was uniformly distributed through the specimen. The results of these tests are detailed in Section 4.1

3.3 Materials Examination Techniques

Microstructural examinations of as-received and pre-fatigued specimens were done with both electron and optical microscopy. Optical microscopy was used to examine each steel's grains structure. Preparation of optical microscopy specimens was accomplished using standard metallographic polishing techniques and the polished surfaces were etched with 2% nital solution for 25 seconds, before observation.

Scanning electron microscope (SEM) specimens required little preparation since only fracture surfaces were examined on this instrument. A JEOL JSM-25 microscope was used at an operating voltage of 25 kV.

The preparation of specimens for the transmission electron microscope (TEM) was more involved than that for SEM or optical microscopy. First, thin discs of metal were cut from as-received and pre-fatigued specimens (within the 1" gauge length) with a low speed diamond saw. These discs, in turn, were punched in a press to obtain smaller 3mm diameter discs. These 3mm discs were ground down to 0.1 mm thickness on 600 grit emery paper, and finally electrolytically polished with a jet pump. The electrolyte was 5% perchloric acid and 95% ethanol. Electrolytic polishing was done at -30°C to -40°C with a voltage of 88V for both SAE 1018 and A533B steels. A JEOL JEM 100C microscope was used at an operating voltage of 100 kV.

4.0 EXPERIMENTAL RESULTS

4.1 Mechanical Testing Results

Impact tests on as-received steels revealed the ductile-brittle behavior of the steels at a temperature range from -200 to 100°C as seen in Figure 4.1. A533B Class II had a temperature transition at approximately -72°C and an upper shelf energy greater than 169.5 J (125 ft-lbs). A533B Class I had a temperature transition at approximately -25°C and an upper shelf energy greater than 169.5 J (125 ft-lbs). The ductile-brittle transition temperature for SAE 1018 was approximately 35°C and it had an upper shelf energy of approximately 135.6 J (100 ft-lbs.). All fatigue and tensile tests on SAE 1018 were run at room temperature (25°C), and at this temperature the steel is in the lower shelf region of the Charpy curve with an impact strength of approximately 18 ft.lbs. The A533B steels were tested at 25°C and at 300°C, and at both these temperatures the steels are on the upper shelf of the curve at approximately 169.5 J (125 ft-lbs.).

Rockwell hardness values for as-received specimens are listed in Table 4.1

Both SAE 1018 and A533B steels were fatigued at a stress amplitude of 207 MPa (30 ksi) with a zero mean stress in the elastic regime (fully reversed). A typical stress-strain plot (or hysteresis loop) for SAE 1018, A533B Class I & II steels, from 10^0 to 10^6 cycles can be seen in Figure 4.2. Since the fatigue occurs in the elastic region there is no plastic deformation and the stress-strain plot is a straight line.

Following fatigue, specimens were either tensile tested, notch-tensile tested or cut for TEM examination. Results of the tensile and notch-tensile tests on as-received and pre-fatigued specimens of SAE 1018, A533B Class I, and A533B Class II are compiled in Tables 4.2, 4.3, and 4.4.

Plots of cyclic (incremental over-strain) tests on as-received specimens, and monotonic tensile tests on as-received and pre-fatigued specimens are shown in Figures 4.3, 4.4, and 4.5. Figure 4.3 shows that SAE 1018 steel cyclicly hardens, but with increasing cycles of fatigue at room temperature the same steel softens. Both A533B Class I & II steels cyclicly soften during incremental over strain tests, but show no effects from fatigue on following tensile tests (see Figure 4.4 and 4.5).

The ultimate strengths of SAE 1018 in Table 4.2 for tensile tests on as-received specimens and specimens pre-fatigued to 10^4 and 10^6 cycles were 583.6 MPa (84.639 ksi), 536.3 MPa (77.925 ksi), and 513.25 MPa (74.438 ksi), respectively. The fracture stresses were 365.4 MPa (53.0 ksi), 375.1 MPa (54.4 ksi), and 358.5 MPa (52.0 ksi), also corresponding to as-received, 10^4 and 10^6 cycles. Results of notch-tensile tests on SAE 1018 in Table 4.2 show a marked decrease in fracture stress with increased levels of fatigue, from 468.9 MPa (68.0 ksi) for as-received specimens, down to 13.8 MPa (2 ksi) for specimens pre-fatigued to 10^6 cycles. These trends are shown in Figure 4.6.

The ultimate strengths of A533B Class I specimens tensile tested were from 627-634 MPa (91-92 ksi) for as-received and pre-fatigued specimens at room temperature, and from 600-607 MPa (87-88 ksi) for tensile tests at 300°C. (See Table 4.3). (Note: only specimens pre-fatigued at 300°C were tensile tested at 300°C). The fracture stresses for Class I at room temperature and at 300°C varied only slightly in the range of 386-400 MPa (56-58 ksi). (See Figure 4.4)

For A533B Class II material, tensile tests yielded ultimate strengths decreasing from 719.1 MPa (104.3 ksi) to 711.6 MPa (103.2 ksi), and to 684.0 MPa (99.2 ksi) for as-received specimens, and specimens pre-fatigued to 10^4 and 10^6 cycles at room temperature. This trend is not observed at 300°C or for notch-tensile tests at either temperature. (See Figures 4.5 and 4.6)

As-received specimens of all three steels showed a discontinuous yielding phenomena, but only specimens of A533B Class II showed this behavior during tensile tests after fatigue at room temperature.

Notch tensile curves for as-received and pre-fatigued SAE 1018, A533B Class I and A533B Class II steels are shown in Figure 4.6. All three of these steels exhibit more ductile behavior after fatigue at room temperature. The A533B steels show even greater ductility after fatigue at 300°C. SAE 1018 specimens pre-fatigued to 10^6 cycles fractured during notch-tensile tests at a displacement 36% greater than that of as-received specimens. A533B Class I specimens fatigued at room temperature fractured at a displacement approximately 25% greater than that of as-recieved, and fractured at a displacement approximately 58% greater at 300°C. A533B Class II specimens fractured at a displacement approximately 56% greater than as-received material, when fatigued to 10^6 cycles at 300°C then notch-tensile tested.

Incremental over-strain tests to 1% strain were run to determine the cyclic stress-strain curves of SAE 1018, A533B Class I, and A533B Class

II steels. Plots of maximum-minimum points and hysteresis loops are shown in Figures 4.7, 4.8, and 4.9, respectively. As stated previously SAE 1018 cyclicly hardens, while the A533B steels cyclicly soften during an incremental over-strain test.

Diamond pyramid hardness (D.P.H.) tests using a Tukon microhardness tester performed on as-received and prefatigued specimens of SAE 1018 and the A533B steels. The mean hardness values, plus or minus one standard deviation, for specimens at each fatigue level are plotted in Figure 4.10. The microhardness values for SAE 1018 vary with different fatigue levels, but show no consistent trend. The A533B Class I steel shows increasing hardness with fatigue at room temperature and at 300°C, from about 200 D.P.H. to 235 D.P.H. A533B Class II shows a consistent drop in microhardness with fatigue and incremental over-strain from 260 D.P.H. for as-received specimens, decreasing to 220 D.P.H. for IOVST (incremental over-strain) specimens.

Microhardness was tested across the diameter of cross-sectioned specimens. No trends were observed when these values were plotted versus the radial distance from the center of the specimen. Thus the steels did not harden or soften in selective areas, but changed uniformly across the specimen. This fact is important in that the location of specimens cut from the gauge length for TEM work was of little consequence; the relatively uniform hardness indicates that there was a uniform dislocation distribution.

4.2 Microstructural Observations

The grains structures of as-received SAE 1018, A533B Class I and II steels are shown in Figure 4.11. The grain sizes of SAE 1018 are much larger than the A533B steels. The gray grains of SAE 1018 are ferrite, while the darker grains are pearlite. The average grain size of SAE 1018 is 25 μm. The A533B steels have a much finer grain structure, which consists primarily of bainite with small quantities of ferrite, and martensite. They have an average grain size of 5 μm.

Optical micrographs of SAE 1018 were taken of as-received and pre-fatigued specimens to see if any microstructural changes could be observed due to fatigue cycling. As seen in Figure 4.12 no structural changes were observed by optical microscopy. Due to the much smaller grain size of the A533B steels, it was difficult to see any detail at magnifications achieveable with an optical microscope.

Scanning electron microscope (SEM) micrographs of the fracture surfaces of notch-tensile specimens of SAE 1018 are shown in Figure 4.13. The as-received specimen behaved in an almost brittle manner when compared to specimens pre-fatigued to 10^4 and to 10^6 cycles. This is clearly shown in SEM micrographs in Figure 4.13. At room temperature, SAE 1018 is almost at the lower shelf in the brittle region of the Charpy curve. This should explain the brittle tensile behavior. The fracture surface of the SAE 1018 as-received specimen shows evidence of brittle failure by transgranular cleavage fracture. When SAE 1018 specimens are fatigued to 10^4 and to 10^6 cycles, they show predominately ductile behavior fracturing by microvoid coalescence during a notch-tensile test. It is possible that fatigue shifts the brittle fracture mechanism to lower temperatures, and this could be related to a similar change in Charpy impact behavior. The SEM micrographs for the A533B steels all show ductile failure. At room temperature and higher temperatures these steels are on the upper shelf region of the charpy impact curve in the ductile region. Figure 4.5 shows an increase in ductility due to fatigue for A533B steels, but the SEM micrographs did not reveal any observable changes in notch-tensile fracture surfaces. (See Figures 4.14 and 4.15)

Transmission electron microscopy (TEM) was utilized to observe any microstructural changes that occured due to fatigue, that were not detected using optical microscopy. TEM micrographs of SAE 1018 as-received steel showed the typical ferrite-pearlite grain structure with an average grain size of 25 μm. (See Figure 4.16A) As-received specimens are relatively dislocation free and the Fe_3C laths in the pearlite grains are unbroken. Micrographs of SAE 1018 fatigued to 10^4 cycles (see Figure 4.16B) and to 10^6 cycles (see Figure 4.16C) show an increase in dislocation density and the initiation of dislocation cells in the ferrite grains. Specimens of SAE 1018 from incremental over-strain tests to 1% strain showed a marked increase in dislocations generating subgrain boundaries (see Figure 4.16D). The average subgrain size was 0.97 μm.

TEM micrographs of A533B Class I steel revealed grains of ferrite, martensite, and bainite packets and laths, as well as carbide particles and some carbide laths. The average grain size of as-received specimens was approximately 5 μm (see Figure 4.17A). Specimens fatigued to 10^4 cycles at room temperature (see Figure 4.17B) and to 10^4 at 300°C (see Figure 4.17C) show a large increase in dislocation density and the initial generation of dislocation cells. Incremental over-strain specimens have an even greater number of dislocations and they have well formed subgrains with an average size of 0.68 μm.

As-received specimens of A533B Class II have a grain size of approximately 5 μm (see Figure 4.18A), with a fairly low dislocation density. After fatigue to 10^4 cycles at room temperature (see Figure 4.18B) and to 10^4 cycles at 300°C (see Figure 4.18C) specimens had an increased dislocation density again showing the generation of tangles of dislocations into dislocation cells. The tangles of dislocations are more prominent in incremental over-strain specimens, and clearly define subgrains with an average size of 0.67 μm.

An analysis of carbide particle size was performed on TEM micrographs of all three steels with an Imanco "Quantimet 720" image analyzing computer. A carbide size distribution for each steel can be seen in Figure 4.19. One important point to note is that while SAE 1018 steel has an average grain size five times that of the A533B steels, all three steels have roughly the same size carbides with very similar carbide size distributions. No analysis was performed to determine the chemical composition of the carbides present in each steel.

5.0 DISCUSSION

5.1 Suppression of the Yield Point by Fatigue Cycling

The experimental results establish that the sharp yield point can be suppressed or eliminated by subjecting the three steels to fully reversed cyclic pre-fatigue at 207 MPa (30 ksi) in the elastic regime. For the A533B steels, the elimination of the yield point occurs only when fatigued and tensile tested at 300°C. The elimination of discontinuous yielding has also been reported by Abel and Muir(33) and by Klesnil and Lukas(32) in low-carbon steels after fatigue at stress amplitudes slightly lower than the macroscopic yield point. This differs from our procedure since the SAE 1018 and the A533B steels were fatigued at a stress amplitude much lower than the yield point. Holden(31) also found an elimination of discontinuous yielding in mild steel after cycling at or below the fatigue limit using a coaxing procedure. In SAE 1018, the change to continuous yielding can be attributed to the 10^4 or 10^6 cycles of fatigue creating mobile dislocations and thus rapid strain propagation. In the stress-strain plots for the A533B steels, the elimination of the yield point occured only at 300°C and there was no detectable difference between as-received and pre-fatigued specimens. Here the elimination of the yield point can only be explained by the increased temperature, which also leads to mobile dislocations and continuous yielding.

5.2 Softening of SAE 1018 by Elastic Cyclic Fatigue

The effect of fatigue on the plain carbon steel SAE 1018 is an increased level of softening with increasing cycles of stress. This softening effect is seen during subsequent tensile tests in Figure 4.3, but was not verified with diamond pyramid microhardness tests. Studies by Polakowski and Palchoudhuri[22] and by Klesnil and Lukas[32] also reported softening of certain metals under the action of fatigue loading. Klesnil and Lukas state that softening is caused by expansion of deformed zones created during plastic cycling. The motion of free dislocations within these zones contributes to the total plastic strain. This is a plausible explanation and would help account for our observed microhardness measurements, in that the diamond indenter was larger than any of the subgrains seen in these steels, therefore changes in hardness could not be detected within subgrains. Only an average hardness was obtained over a number of these subgrains.

Tensile tests on pre-fatigued A533B steels did not show any softening when compared to as-received material. But on subsequent notch-tensile tests, the A533B steels showed a similar increase in ductility to that seen in notch-tensile tests on SAE 1018.

5.3 Increased Ductility During Notch-Tensile Tests

As seen in Figure 4.6 both SAE 1018 and the A533B steels exhibit more ductile behavior during notch-tensile tests after being fatigued in the elastic regime at room temperature. The A533B Class I and II steels showed even more ductile behavior at 300°C. No other studies were found that examined changes in ductility (as in notch-tensile tests) due to pre-fatigue. But an investigation by Li and Leslie[28] has shown that increasing the amount of pre-strain up to 9% markedly increases yield and ultimate tensile strengths, however, the ductility decreases drastically.

5.4 Notch-Ductile-Brittle Behavior of SAE 1018 and A533B

After fatigue cycling at room temperature at 10^4 or 10^6 cycles SAE 1018 showed more ductile behavior as evidenced in notch tensile tests and in post test examination of the fracture surfaces (see Figures 4.6 and 4.13). This change from brittle to ductile behavior could be explained if it can be shown that fatigue in the elastic regime shifts the brittle fracture mechanism to lower temperatures. This could be related to a shift to lower temperatures in Charpy V-notch impact behavior. At room temperature the pre-fatigued steel would then be on the upper shelf of the curve and would thus exhibit ductile behavior. Due to constrictions on size of Charpy specimens, no impact tests were performed after pre-fatigue; this hypothesis remains to be tested.

Studies by Li and Leslie(28) have shown that pre-straining by dynamic strain aging on low-carbon steels shifts the ductile-brittle transition temperature up by as much as 16°C (29°F). This change is opposite that which would explain the increase in ductility in SAE 1018, but their steels strain harden, as opposed to the softening of SAE 1018.

A study by Holden(31) found that fatiguing mild steels, using a coaxing procedure, resulted in a large increase in the ductile-to-brittle transition temperature during notched impact tests of the fatigued material.

Li and Leslie's(28) studies of SAE 1020 steel (very similar in chemical composition and mechanical properties to SAE 1018) showed a marked increase in tensile yield strength for specimens pre-strained to 3% when compared to as-rolled material. This was accompanied by the aforementioned increase in ductile-brittle transition temperature. The results of our investigation of SAE 1018 showed a drop in yield stress from 363.8 MPa (52.766 ksi) for as-received specimens to 328.6 MPa (47.653 ksi) for specimens pre-fatigued to 10^6 cycles at a stress amplitude of 207 MPa (30 ksi) or approximately 0.1% (elastic) strain. The drop in ultimate strength was even greater (see Table 4.2). Since pre-fatigue causes drops in yield strength and in ultimate strength, as opposed to increases seen in tensile tests of pre-strained steel, it might be expected to decrease the ductile-brittle transition temperature, thus providing an explanation for the appearance of the SAE 1018 notch-tensile fracture surfaces in Figure 4.13.

Though the A533B steels show no softening during tensile tests after fatigue at room temperature or at elevated temperature, they do exhibit softening during incrmental over-strain tests. This could be related to a yield point drop or suppression and thus it might be expected to shift the ductile-brittle transition to lower temperatures.

5.5 Dislocation Subgrains & Cell Structure

It has been shown that cyclic fatigue in the elastic regime causes an increase in dislocation density and the congregation of dislocations into tangles, thus creating dislocation cells within metal grains (see Figures 4.16, 4.17, and 4.18). Examination of the microstructure of the SAE 1018 and A533B steels, after incremental over-strain tests to 1% strain, revealed tangles of dislocations which were more clearly defined. These tangles divided the grains into subgrains with cell sizes averaging from 0.97 μm for SAE 1018, 0.68 μm for A533B Class I, and 0.67 μm for

A533B Class II. The density of dislocations in the interior of the subgrains is very low. The generation of subgrains by interconnecting dislocation tangles has also been reported by Abdel-Raouf and Plumtree,[23] Ivanova. et al.,[43] and by Klesnil and Lukas.[44] Klesnil and Lukas also reported the formation of polygonally shaped cell structure during high strain amplitude (life $N < 10^5$) fatigue. It is the motion of dislocations within the subgrain structure that Klesnil and Lukas used to account for fatigue induced softening. This polygonic cell structure was formed in SAE 1018 and the A533B steels during incremental over-strain tests as seen in Figures 4.16D, 4.17D, and 4.18D.

5.6 Carbide Dependent Fracture

Curry and Knott's[15,16,&19] studies show there is a general relation between ferrite grain size, largest observed carbide particle size, and cleavage fracture stress in mild steels. As seen in Figure 2.3 they proposed a non-linear grain size versus fracture stress dependence with an effective surface energy $\gamma_p = 14\ \mathrm{Jm^{-2}}$. Predictions of cleavage fracture stress based on $d^{-1/2}$, where d is the grain size from Figure 2.3 for the SAE 1018 and A533B steels as well as for steels investigated by McMahon and Cohen,[10] Groom and Knott,[45] and Oates[46] are compiled in Table 5.1.

A straight line dependence between grain size and cleavage fracture stress is proposed by Brozzo et al.[47] for low-carbon bainitic steels with a carbon content less than 0.05%. This straight line dependence is also shown in Figure 2.3. Brozzo et al. calculated a

γ_p = 120 N/m for their data based on the Griffith-Orowan relation written as Eq. [2] in their paper. A reanalysis of their data using an $E = 2.07 \times 10^{11}$ N/m^2, $\nu = 0.3$, and their values for σ_f and d gives a value of γ_p = 38 N/m.

Curry and Knott found that in materials where the cracking of intragranular or grain boundary carbides was the key event which determined fracture, that the Griffith mechanism did not appear to be active. They suggested that the fracture mechanism should be that proposed by Smith(48) and that the observed dependence of σ_f on $d^{-1/2}$ is really a consequence of the dependence of σ_f on carbide thickness. A modified version of Smith's equation is Eq. [5] in Chapter 2. Though this equation is valid for predicting fracture stress in steels fracturing due to cracking grain boundary carbides (through thickness-cracks) it does not hold for steels where fracture is controlled by intragranular spheroidal carbides.

In Curry and Knott's(16) research of spheroidal carbides they developed two simplified equations to predict cleavage fracture. They are:

$$\sigma_f = \left[\frac{\pi E \gamma_p}{2(1-\nu^2)r}\right]^{1/2} \qquad [7]$$

for penny-shaped cracks in intragranular spheroidal carbides, and

$$\sigma_f = \left[\frac{2 E \gamma_p}{\pi(1-\nu^2)r}\right]^{1/2} \qquad [8]$$

for through-thickness cracks in grain boundary carbides. The grain boundary carbide thickness is represented by $C_0 = 2r$. They found that if the average radius of the largest 5% of observed carbide particles was used in the Griffith crack propagation criteria Eq. [7] or Eq. [8] for calculation of cleavage fracture stress, due to the propagation of penny-shaped or through thickness crack nuclei, results were found to be in good agreement with their own experimental results.

Fracture stress, grain size, and carbide size values were extracted from works by McMahon and Cohen,[10] Groom and Knott[45] and Oates[46]. Using these values, a predicted fracture stress as a function of d was determined for each steel using Figure 2.3 and Curry and Knott's Curve with a γ_p = 14 N/m. It must be noted that this curve is based on Eq. [5] developed by Smith,[48] which encompasses both grain size and carbide size effects. Then carbides sizes, r, reported by the investigators above were used in conjunction with Curry and Knott's[16] relation dependent only on carbide size. Equation [8] is only a slight modification of Griffith's equation, where a $r^{-1/2}$ dependence has been substituted for a $d^{-1/2}$ dependence. A comparison of the fracture stresses determined by these two methods is shown in Table 5.1 along with experimentally determined values. Both methods seem to provide adequate predictions of cleavage fracture stress for the steels they dealt with.

An analysis of carbide particle size was made on SAE 1018, A533B Class I, and A533B Class II steels to determine whether or not accurate estimates of cleavage fracture stress, using Curry and Knott's method, could be made on these low-carbon steels. Carbide particle radii distributions were determined for each steels microstructure using an Imanco "Quantimet 720" image analyzing computer* (see Figure 4.19).

*Facility provided by the U.S. Army Construction Engineering Research Laboratory, Champaign, Illinois 61820.

Analysis was performed on TEM micrograph negatives and approximately 250 carbides were measured for each steel.

The average radius of the largest 5% of the carbide particles was .0821 μm for SAE 1018, .0834 μm for A533B Class I, and .0831 μm for A533B Class II. Fracture stresses were calculated using Eq. [7] and values of E=207 GPa, γ_p=14 N/m, ν=0.3 and the above values of r. The predicted cleavage fracture stress values in the temperature range from -130 to -150°C were 7,897 MPa (1,145 ksi) for SAE 1018; 7,745 MPa (1,123 ksi) for A533B Class I; and 7,758 MPa (1,125 ksi) for A533B Class II. These values are tabulated in Table 5.1.

It can be seen in Figure 2.2 and in work by Griffith and Owen(49) that fracture stress is relatively insensitive to temperature. Then values of fracture stress obtained through room temperature tensile tests should be close to low temperature cleavage fracture stress values. As seen in Table 5.1, the actual fracture stress values for the SAE 1018 and A533B steel obtained at room temperature range from 827 MPa to 1379 MPa. These values are much closer to those predicted by grain size dependence than by the carbide size dependence as proposed by Curry and Knott.(16)

Fracture stress values reported by Groom and Knott,(45) Oates,(46) and McMahon and Cohen(10) show a much closer agreement between grain size and carbide size predictions with those they determined by experimentation. The carbides they observed were on the order of 10 to 60 times larger than those seen in the low-carbon steels studied here. This may be one reason Curry and Knott's relation does not give accurate fracture stress estimates for these steels.

Finally, Figure 2.3 and the results shown in Table 5.1 indicate that there are two competing fracture mechanisms (carbide-controlled, grain-size controlled) operating over the entire range of grain diameter d values in ferritic steels. At relatively low values of $d^{-1/2}$ the literature tends to indicate that the first mechanism by Smith[48] predominates, but for higher values of $d^{-1/2}$ Brozzo et al.[47] suggest that the Griffith mechanism would take over. But the analysis of the SAE 1018 and A533B steels indicates that even at the higher values of $d^{-1/2}$ the Smith mechanism, based on both grain size and carbide size, will give better predictions of cleavage fracture stress. An analysis of these steels also revealed that accurate estimates of fracture stress can not be made with the relation based solely on carbide size effects. In general, for steels with large carbides the Griffith mechanism predominates, but in steels with relatively small carbides the Smith mechanism predominates. Thus, the cleavage fracture stress is determined using the appropriate mechanism.

6.0 CONCLUSIONS

I. Three types of steels with similar low-carbon compositions were tested. SAE 1018 was ferritic and pearlitic with an average grain size of 25 μm, and both A533B Class I and II were primarily bainitic with small amounts of ferrite and martensite with average grain sizes of 5 μm.

II. Fatigue in the elastic regime at room temperature causes SAE 1018 to soften, while incremental over-strain results in hardening. At 25°C SAE 1018 is almost on the lower shelf of the Charpy impact curve at approximately 18 ft-lbs. where it exhibits mostly brittle behavior.

II. A533B Class I and II steels cyclically soften in an incremental over-strain test, but show no real change in monotonic tensile properties due to fatigue. At 25°C and at 300°C the A533B steels are on the upper shelf of the Charpy curve and exhibit fully ductile behavior with an impact energy of approximately 120 ft-lbs.

IV. In notch-tensile tests both SAE 1018 and A533B steels behave in a more ductile manner after being fatigued in the elastic regime. This increase in ductility is more pronounced after fatigue at elevated temperature (300°C) for A533B steels.

V. SEM fractography of SAE 1018 notch-tensile specimen fracture surfaces shows a change from semi-brittle to predominately ductile behavior after fatigue to 10^4 and to 10^6 cycles at 207 MPa (30 ksi).

VI. The upper yield point of SAE 1018 steel disappears with fatigue in the elastic regime at room temperature.

VII. TEM micrographs show the formation of dislocation cells in pre-fatigued specimens and subgrains in specimens which had undergone incremental over-strain in both the SAE 1018 & A533B steels. The average cell size (calculated by the linear intercept method) for SAE 1018 was 0.97 μm, 0.68 μm for A533B Class I, and 0.67 μm for A533B Class II.

VIII. After comparison of microstructural data with various fracture theories it was shown that to make accurate estimates of cleavage fracture stress both grain size and carbide size effects must be taken into account.

TABLES

Table 2.1 Prior Research Investigations

Reference No.	Researcher	Materials Studied	Tests
1.	Griffith	Glass	Theories of Rupture and experimental verification
2.	Ludwik	-	Brittle Fracture Theory
3.	Orowan	-	Theory of Brittle Behavior
4.	Eldin & Collins	Hot coiled 1020 steel	Low Temperature Tensile Tests
5.	Wessel	Rimmed Structural Steel ABS-A(.24%C)	Notched Tensile Tests (low temperature)
6.	Cottrell	-	Brittle Fracture Theory
7.	Low	Low carbon steel	Tensile Tests (low temperature)
8.	Parker	.2% carbon steel	Tensile Tests -400 to 500°F
9.	Hahn	Low carbon steel(.22%C)	Low Temperature Tensile & Impact Tests
10.	McMahon & Cohen	Low-carbon Iron	Low Temperature Tensile Tests
11.	Lindley,Oatcs,&Richards	Low-carbon Iron	Tensile Tests, Carbide cracking mechanisms
12.	Man,Vlach,& Holzman	Low carbon steel CSN 12013(.6%C)	Low Temperature tensile tests
13.	Richie,Knott,& Rice	High Nitrogen mild steel	Bend Tests, Fracture Toughness Tests
14.	Richie,Server,&Wullaert	Low carbon alloy steels A533BI,A302B	Fracture Toughness Tests
15.	Curry & Knott	High Nitrogen mild steel (.10%C)	Fracture Toughness Tests Cleavage Fracture Theories
16.	Curry & Knott	Plain carbon steels	Notch Bend Tests
17.	Curry & Knott	1% Carbon tool steel & low alloy steel	Fracture Toughness Tests
18.	Curry	-	Comparison of Richie,Knott, Rice & Curry-Knott Fracture Models
19.	Curry	-	Cleavage micromechanism Theories

Table 2.1 Prior Research Investigations (Cont.)

Reference No.	Researcher	Materials Studied	Tests
20.	Knott	-	Micromechanisms of fiborous crack growth
21.	Curry	bainitic pressure-vessel steel A508 class II	Cleavage fracture
22.	Polakowski&Palchoudhuri	Copper,Tin-bronze,Ti-steel,Cupro-nickle, aluminum	High Stress Fatigue
23.	Abdel-Raouf & Plumtree	Polycrystal-line "Ferro-vac E" Iron	Fatigue cycling
24.	Sinclair	Ingot iron SAE1045,234C 75S-T6 alumi-num alloy, 70-30 Brass	Coaxing
25.	Krommers	Armco Iron & SAE 1020	Understressing and overstressing
26.	Mintz & Wilson	Low carbon, mild & .7% carbon steel	Strain aging
27.	Wilson & Tromans	Low carbon rimming steel (.03%C)	Strain aging
28.	Li & Leslie	AISI 1008,1020 1522,&1035 steels	Strain aging
29.	LeMay	-	Bauschinger Effect Theory
30.	Steichen & Williams	Low carbon alloy steel A533B class I	Strain rate & temperature dependence of tensile prop
31.	Holden	Mild steel (.09%C)	Cyclic Stressing at Fatigue Limit
32.	Klesnil & Lukas	Low carbon steel(.07%C)	Fatigue Softening and Hardening
33.	Abel & Muir	Fully killed low carbon steel(.17%C)	Cyclic Loading and subsequent tensile tests
34.	Cottrell & Bilby	-	Dislocation & Strain aging Theories
35.	Cottrell	-	Fracture Theories
36.	Cottrell	-	Fracture Theories

Table 2.1 Prior Research Investigations (Cont.)

Reference No.	Researcher	Materials Studied	Tests
37.	Johnston & Gilman	Lithium Fluoride crystals	Dislocation Velocities, Densities & Plastic Flow
38.	Hahn	Iron & BCC metals	Tensile Tests, Model for Yielding
39.	Abel & Muir	Fully Killed hot-coiled low carbon steel(.17%C)	Bauschinger Effect and discontinuous yielding
40.	Mader, Seeger, & Leitz	Nickel & Nickel-cobalt alloy single crystals	Work Harding
41.	Orowan	-	Internal Stress Theory
42.	Kaufman, Sha, Kohn, & Bucci	Aluminum alloys 2024, 2124, 7075, & 7475	Notch Tensile/K_{IC} correlations

Table 3.1 Chemical Compositions of A533B and SAE 1018 steels

CHEMICAL COMPOSITIONS (weight %)

Element	A533B Class I*	A533B Class II**	SAE 1018***
Carbon	.19	.193	.18
Manganese	1.32	1.340	.82
Phosphorus	.013	.008	.012
Sulfur	.013	.003	.016
Silicon	.22	.210	<.05
Molybdenum	.54	.500	<.03
Nickel	<.05	.600	<.05
Copper	.12	.070	.24
Chromium	<.05		<.05

* Donated by Combustion Engineering, Inc.
** Supplied by Creusot-Loire, France
*** Supplied by U.S. Steel, Inc.

TABLE 3.2 SPECIFICS OF EXPERIMENTAL PROCEDURE

- FATIGUE TESTS
  - FULLY REVERSED FATIGUE TESTS
  - CYCLING BELOW CRACK INITIATION IN THE ELASTIC REGION
  - LOAD CONTROLLED TESTS

    STRESS AMPLITUDE = $\pm$ 30 ksi ($\simeq$ 0.1 % Strain)

    MEAN STRESS = 0.0 ksi

    FREQUENCY = 7.5 Hz
  - 10^4 CYCLES & 10^6 CYCLES (actually 1.638×10^4 & 1.048×10^6 cycles)
  - ROOM TEMPERATURE ON SAE 1018
  - ROOM TEMPERATURE & 300°C FOR A533B CLASS I & II

- TENSILE & NOTCH-TENSILE TESTS
  - COMPUTER CONTROLLED (REAL TIME)

    0-10% STRAIN = STRAIN CONTROLLED

    < 10% STRAIN = STROKE CONTROLLED
  - STRAIN RATE = 0.0005/second
  - ROOM TEMPERATURE ON SAE 1018
  - ROOM TEMPERATURE & 300°C ON A533B CLASS I & II (all notch-tensile tests at room temperature)

- IMPACT TESTS (AS-RECEIVED)
  - STANDARD SIZE CHARPY BLOCKS
  - TEMPERATURE RANGE FROM -196°C TO 100°C

- INCREMENTAL OVER-STRAIN TESTS
  - MAXIMUM STRAIN = 1.0%

- HARDNESS TESTS (AS-RECEIVED)

STEEL \ Fatigue Level	FATIGUE				TENSILE						NOTCH-TENSILE						MICROSCOPY						IOVST (CYCLIC)	IMPACT (CHARPY)	HARDNESS(ROCKWELL)
					RT			300°C			Room Temperature														
	10^4 RT	10^6 RT	10^4 300	10^6 300	AR RT	10^4 RT	10^6 RT	AR 300	10^4 300	10^6 300	AR RT	10^4 RT	10^6 RT	AR 300	10^4 300	10^6 300	AR RT	10^4 RT	10^6 RT	10^4 300	10^6 300	IOVST AR&RT			
SAE 1018	x	x			x	x	x				x	x	x				2* 3	2* 3	2* 3			3	x	x	x
A533BI	x	x	x	x	x	x	x	x	x	x	x	x	x	x	x	x	2* 3	2* 3	2*	2* 3	2*	3	x	x	x
A533BII	x	x	x	x	x	x	x	x	x	x	x	x	x	x	x	x	2* 3	2* 3	2*	2* 3	2*	3	x	x	x

Fatigue

Stress Aplitude = 30 KSI
Mean Stress = 0 KSI
Frequency = 7.5 Hz
Load Controlled
(Elastic Regime)

Tensile & Notch-Tensile

Strain Rate = 5.0×10^{-4}
Strain Controlled to 10%
>10% Stroke Controlled

Legend

AR= As-received (virgin material)
RT= Room Temperature
1 = Optical Microscopy
2 = Scanning Electron Microscopy
3 = Transmission Electron Microscopy
* = Tensile & Notch-Tensile Fracture Surfaces
IOVST= Incremental Over Strain Test (Cyclic Stress Strain Curve)

Table 3.3 Test Matrix

Table 4.1 Rockwell Hardness Tests

STEEL	*HARDNESS (ROCKWELL B)
SAE 1018	55.3 L 53.8 T
A533B Class I**	61.0 L 62.3 T
A533B Class II	63.5 L 64.4 T

* Average of 5 measurements

** Post Weld Heat Treated

L= Longitudinal

T= Transverse

	TENSILE TESTS			NOTCH-TENSILE TESTS		
	As-received	10^4 *	10^6 **	As-received	10^4 *	10^6 **
Elastic Modulus (KSI)	30,255.1	29,333.8	29,297.0	50,812.3	50,602.6	47,376.7
.2% Yield Stress (KSI) @ Strain	52.766 3.439×10^{-3}	48.466 3.566×10^{-3}	47.653 3.547×10^{-3}	78.928 3.488×10^{-3}	79.395 3.468×10^{-3}	74.613 3.468×10^{-3}
Ultimate Strength (KSI) @ Strain	84.639 >0.1	77.925 >0.1	74.438 >0.1	106.795 .038028	109.888 .0449477	103.379 .0431461
Upper Yield Stress (KSI) @ Strain	56.264 >0.1	-	-	-	-	-
Lower Yield Stress (KSI) @ Strain	52.766 3.703×10^{-3}	-	-	-	-	-
Fracture Stress (KSI)	53.0	54.4	52.0	68.0	60.0	2.0
Intitial Spec. Area (sq. in.)	.04987	.04909	.04869	.02717	.02717	.02717
Final Spec. Area (sq. in.)	.01838	.01629	.01629	-	-	-
% Reduction of Area	63.1	66.8	66.6	-	-	-
True Fracture Strain	.9979	1.1033	1.0953	-	-	-
True Fracture Strength (KSI)	135.64	163.94	155.12	-	-	-
True Fracture Strength Corrected to (KSI)	119.74	143.44	136.13	-	-	-
Strain Hardening Exponent	.1778	.1814	.1927	-	-	-
Strength Coefficient (KSI)	122.536	131.578	129.524	-	-	-

Table 4.2 Tensile & Notch-Tensile Results for SAE 1018

* actually 1.638×10^4 cycles
** actually 1.048×10^6 cycles

	TENSILE TESTS (25°C)			TENSILE TESTS (300°C)			NOTCH-TENSILE TESTS (25°C)				
	As-received	10^4cycles*	10^6cycles**	As-received	10^4cycles*	10^6cycles**	As-received	10^4, 25°C	10^6, 25°C	10^4,300°C	10^6,300°C
Elastic Modulus (KSI)	29,746.7	30,037.5	29,615.6	27,701.2	23,131.3	27,253.6	51,670.2	65,581.4	51,702.3	50,330.0	48,862.7
.2% Yield Stress (KSI) @ Strain	72.700 4.328×10^{-3}	73.718 4.425×10^{-3}	72.817 4.397×10^{-3}	64.696 4.192×10^{-3}	65.473 4.201×10^{-3}	65.121 4.299×10^{-3}	119.830 4.211×10^{-3}	120.57 4.162×10^{-3}	120.02 4.211×10^{-3}	120.10 4.299×10^{-3}	116.32 4.289×10^{-3}
Ultimate Strength (KSI) @ Strain	91.280 .09088	92.648 .09353	92.047 .09352	88.326 .08550	87.695 .07803	88.609 .08805	136.736 .02713	138.96 .02609	138.78 .02966	140.45 .03186	136.10 .03587
Upper Yield Stress (KSI) @ Strain	73.70 2.67×10^{-3}	-	-	-	-	-	-	-	-	-	-
Lower Yield Stress (KSI) @ Strain	72.00 3.2×10^{-3}	-	-	-	-	-	-	-	-	-	-
Fracture Stress (KSI)	57.10	57.71	57.14	57.73	56.45	58.18	50.81	33.87	46.55	40.00	35.01
Intitial Spec. Area (sq. in.)	.0513	.0488	.0488	.0513	.0492	.0485	.02717	.02717	.02717	.02717	.02717
Final Spec. Area (sq. in.)	.0163	.0159	.0147	.0161	.0189	.0172	-	-	-	-	-
% Reduction of Area	68.2	67.3	69.9	68.5	61.7	64.5	-	-	-	-	-
True Fracture Strain	1.1468	1.1178	1.2024	1.1565	.5593	1.037	-	-	-	-	-
True Fracture Strength (KSI)	179.76	176.49	190.17	183.52	147.32	153.89	-	-	-	-	-
True Fracture Strength Corrected to (KSI)	156.62	154.24	165.11	159.90	130.49	144.20	-	-	-	-	-
Strain Hardening Exponent	.1335	.1519	.1544	.1403	.1386	.1401	-	-	-	-	-
Strength Coefficient (KSI)	138.72	149.78	150.26	138.28	137.42	138.03	-	-	-	-	-

Table 4.3 Tensile & Notch-Tensile Results for A533B Class I
* actually 1.638×10^4 cycles
** actually 1.048×10^6 cycles

	TENSILE TESTS (25°C)			TENSILE TESTS (300°C)			NOTCH-TENSILE TESTS (25°C)				
	As-received	10^4 cycles*	10^6 cycles**	As-received	10^4 cycles*	10^6 cycles**	As-received	10^4, 25°C *	10^6, 25°C**	10^4, 300°C *	10^6, 300°C**
Elastic Modulus (KSI)	30,427.6	29,869.9	28,933.5	27,240.7	27,710.9	27,149.4	53,591.9	52,500.7	51,175.0	53,120.6	50,125.2
.2% Yield Stress (KSI) @ Strain	87.486 4.76×10^{-3}	86.678 4.89×10^{-3}	83.507 4.86×10^{-3}	76.652 4.74×10^{-3}	76.322 4.75×10^{-3}	76.152 4.74×10^{-3}	136.820 4.47×10^{-3}	136.281 4.47×10^{-3}	135.742 4.55×10^{-3}	135.562 4.49×10^{-3}	137.360 4.72×10^{-3}
Ultimate Strength (KSI) @ Strain	104.291 .09748	103.231 .09338	99.177 .09645	104.958 0.1	104.367 0.1	103.964 .09649	149.226 .01897	149.765 .01979	149.765 .02000	149.406 .01996	153.901 .03166
Upper Yield Stress (KSI) @ Strain	92.191 3.20×10^{-3}	92.677 3.37×10^{-3}	88.179 3.18×10^{-3}	-	-	-	-	-	-	-	-
Lower Yield Stress (KSI) @ Strain	87.197 .01356	86.577 4.48×10^{-3}	82.924 4.30×10^{-3}	-	-	-	-	-	-	-	-
Fracture Stress (KSI)	56.417	58.0	55.0	61.440	66.428	66.659	58.330	83.125	48.0	71.0	37.0
Intitial Spec. Area (sq. in.)	.05087	.04869	.050193	.051432	.048774	.048305	.02717	.02717	.02717	.02717	.02717
Final Spec. Area (sq. in.)	.01227	.01448	.012868	.016038	.017672	.017203	-	-	-	-	-
% Reduction of Area	75.9	70.2	74.4	68.8	63.8	64.4	-	-	-	-	-
True Fracture Strain	1.4219	1.2125	1.2031	1.1653	1.0152	1.0324	-	-	-	-	-
True Fracture Strength (KSI)	233.86	194.99	214.53	197.03	183.34	187.17		-	-	-	-
True Fracture Strength Corrected to (KSI)	200.05	169.18	189.09	171.55	161.60	164.73	-	-	-	-	-
Strain Hardening Exponent	.106311	.13846	.14319	.14075	.14319	.144151	-	-	-	-	-
Strength Coefficient (KSI)	142.966	160.470	155.693	163.048	162.698	162.243	-	-	-	-	-

Table 4.4 Tensile & Notch-Tensile Results for A533B Class II
* actually 1.638×10^4 cycles
** actually 1.048×10^6 cycles

MATERIAL	% Carbon	d (μm)	σ_f^* pred (MPa)	r (μm)	σ_f^+ pred (MPa)	σ_f exp (MPa)	Ref.
SAE 1018	.18%	25	~1,200	.0821	7,897[a]	827	-
A533B Class I	.19%	5	~1,550	.0834	7,745[a]	1,083	
A533B Class II	.193%	5	~1,550	.0831	7,758[a]	1,378	
Mild Steel	.07%	20	~1,250	1.5	1,162[b]	1,114	45
Mild Steel	.06%	55	~1,000	2.25	949[b]	900	46
Manganese Steel	.048%	55	~1,000	1	1,424[b]	1,100	"
Ferrite	.035%	320	~580	5	638[b]	483	10
Ferrite	.007%	250	~625	1.5	1,162[b]	620	"

* Predictions from Figure 2.3 for $\gamma_p = 14\ Jm^{-2}$ curve

\+ Predictions using Curry and Knott's: a= penny-shaped crack Eq. [6]
b= through thickness crack Eq. [7]

Table 5.1 Experimental Versus Predicted Values of Cleavage Fracture Stress

FIGURES

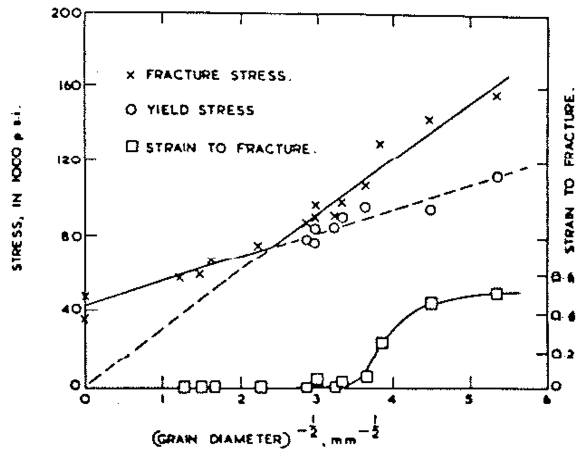

Figure 2.1 Grain size effects on fracture and yield tensile stresses, and on strain to fracture of low carbon steel at -196°C. After Low (7)

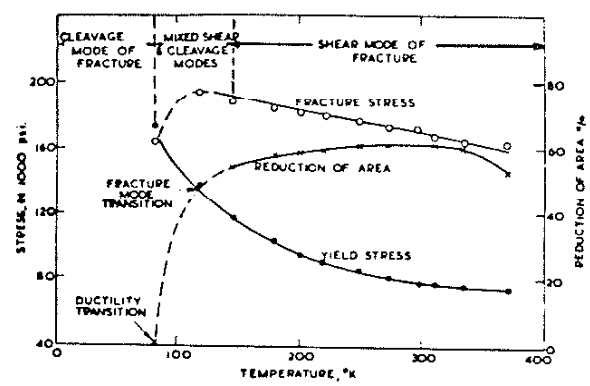

Figure 2.2 Effects of temperature on the true fracture stress, tensile yield stress, and reduction in area, of a low carbon steel. After Parker (8)

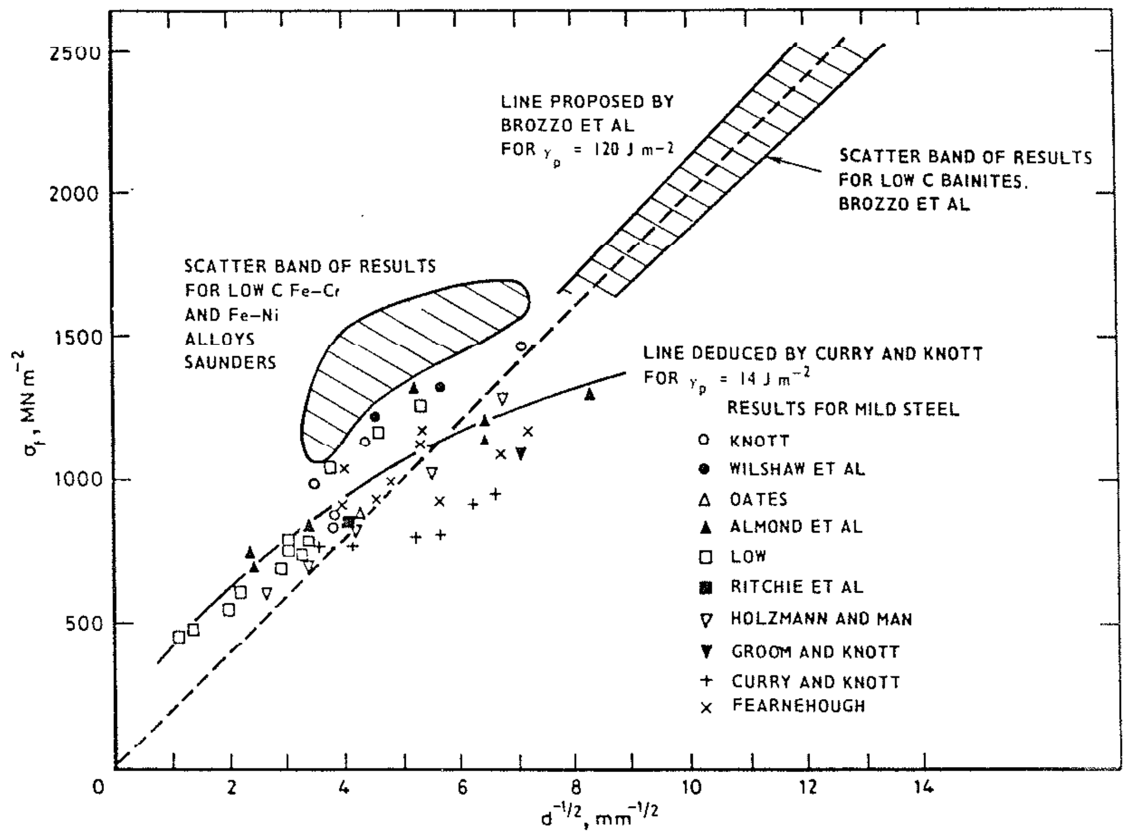

Figure 2.3 Grain size d dependence of cleavage fracture stress σ_f (19)

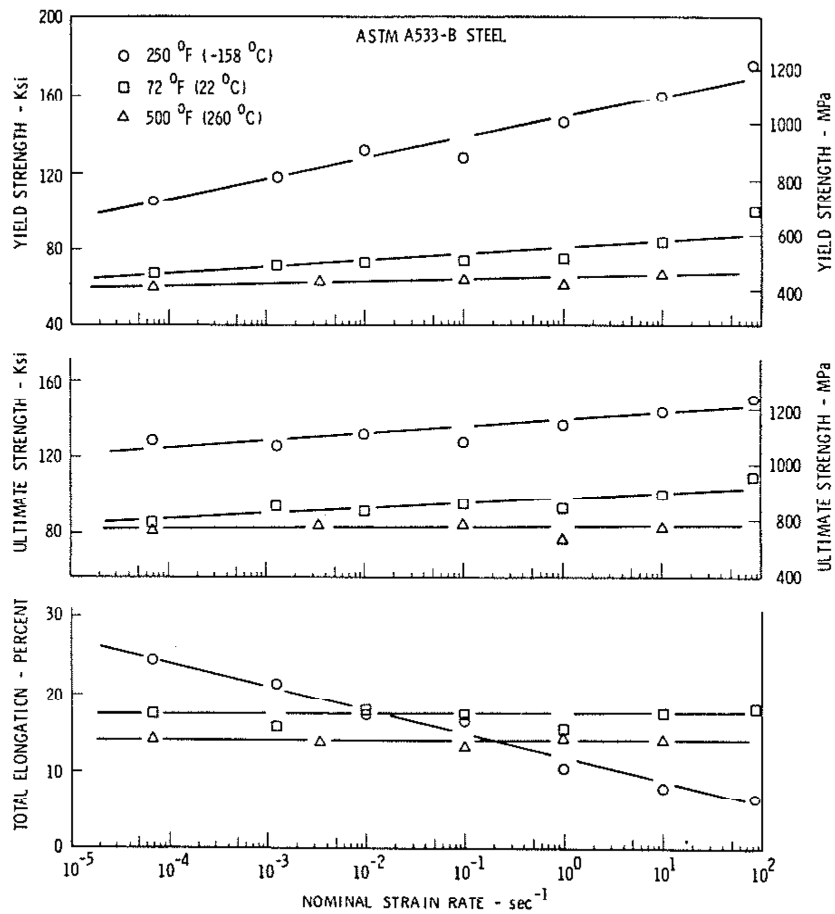

Figure 2.4 Effect of strain rate on the tensile properties of unirradiated ASTM A533, grade B, class 1 steel (30)

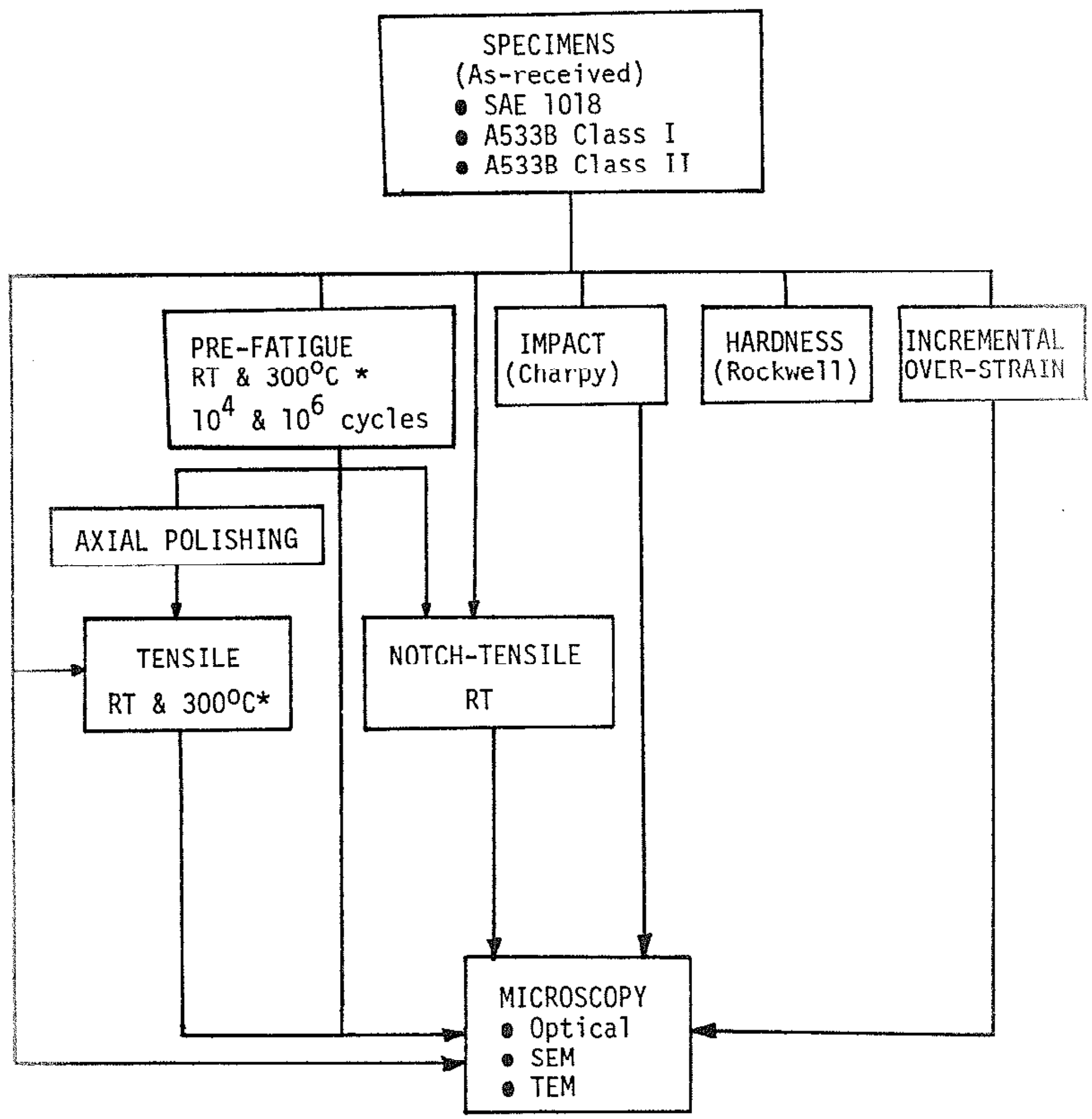

NOTE: * 300°C Testing on A533B Class I & II only
RT = Room Temperature

Figure 3.1 Flow Diagram Of Experimental Approach

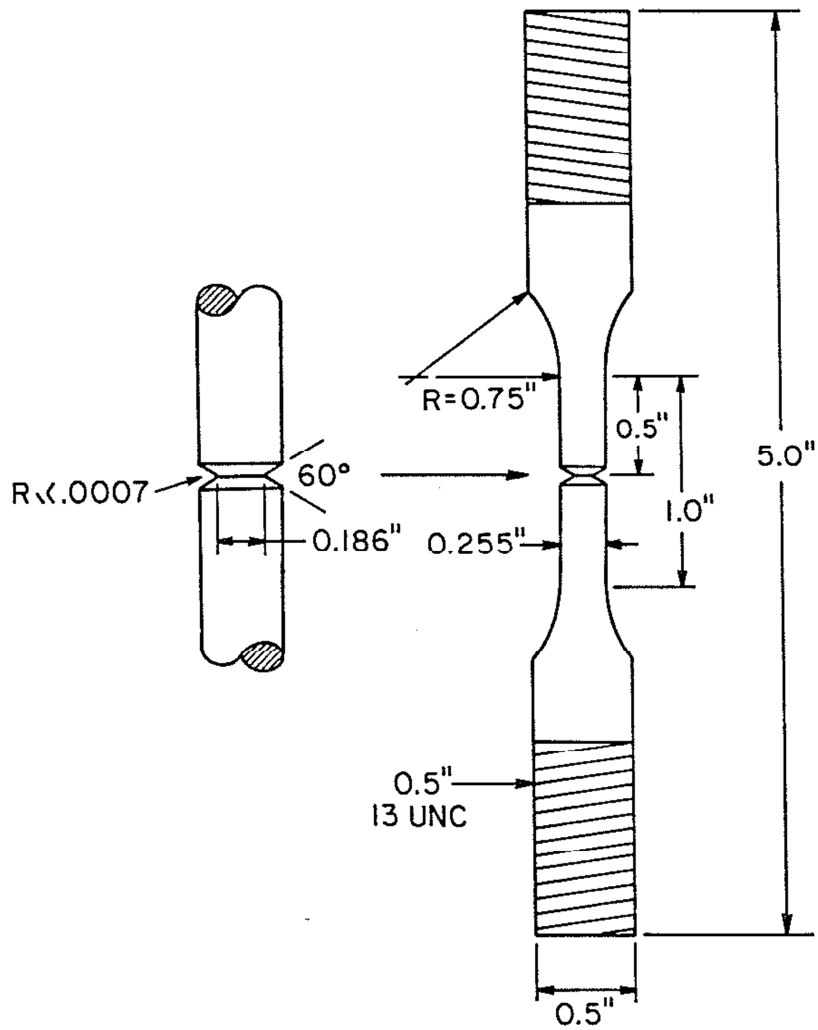

Figure 3.3 Notch-Tensile Test Specimen

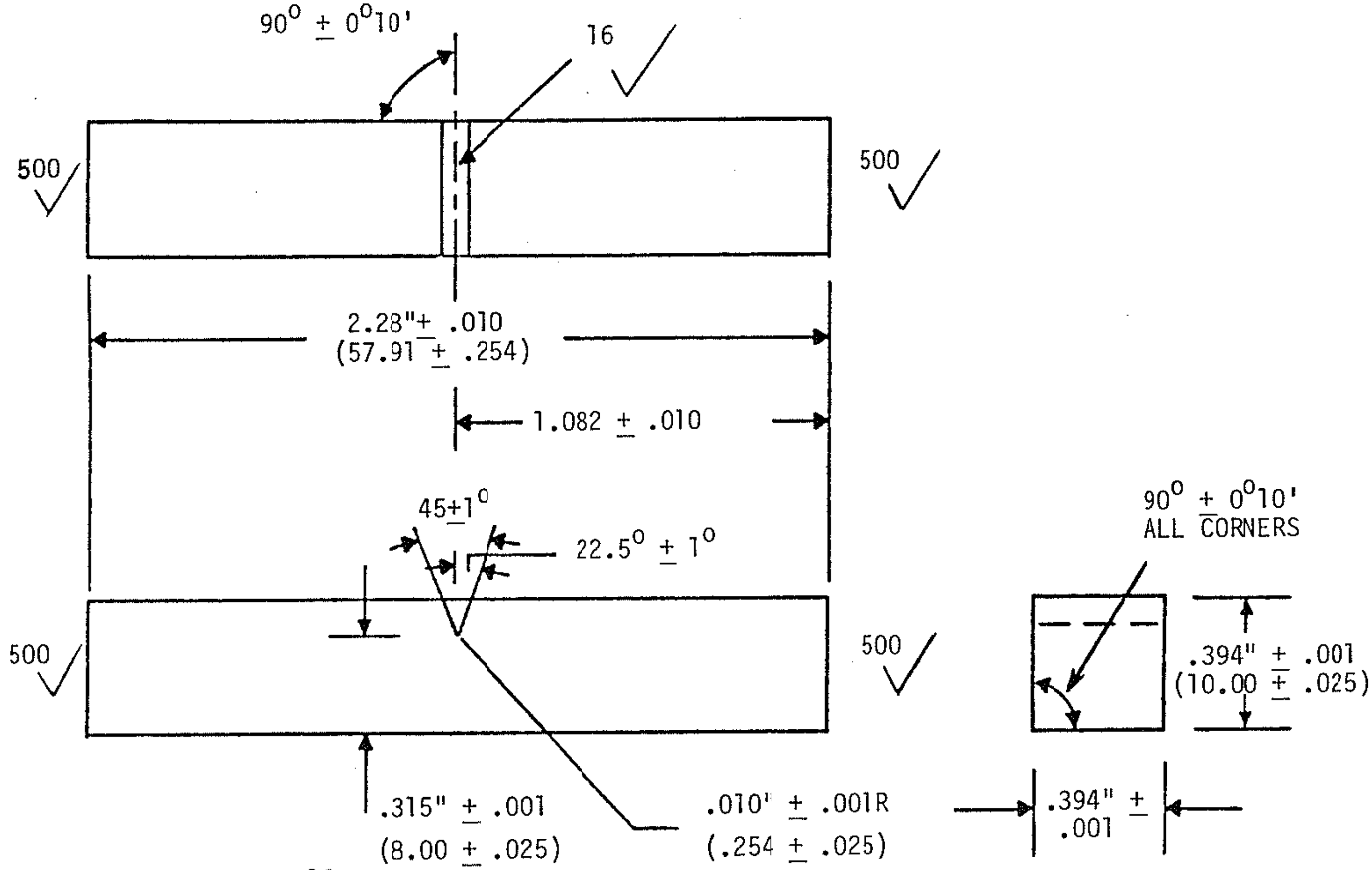

Notes: Notch Area 16✓ and Low Stress Ground
Otherwise 63✓ All Over, Except Ends
Remove All Burrs, Flatness-- no parts of a surface will vary by more than .001 (.025) total indicator reading over entire length. Not required on ends.
Scale: 2:1 Dimensions in inches (mm)

Figure 3.4 Charpy V-Notch Impact Test Specimen

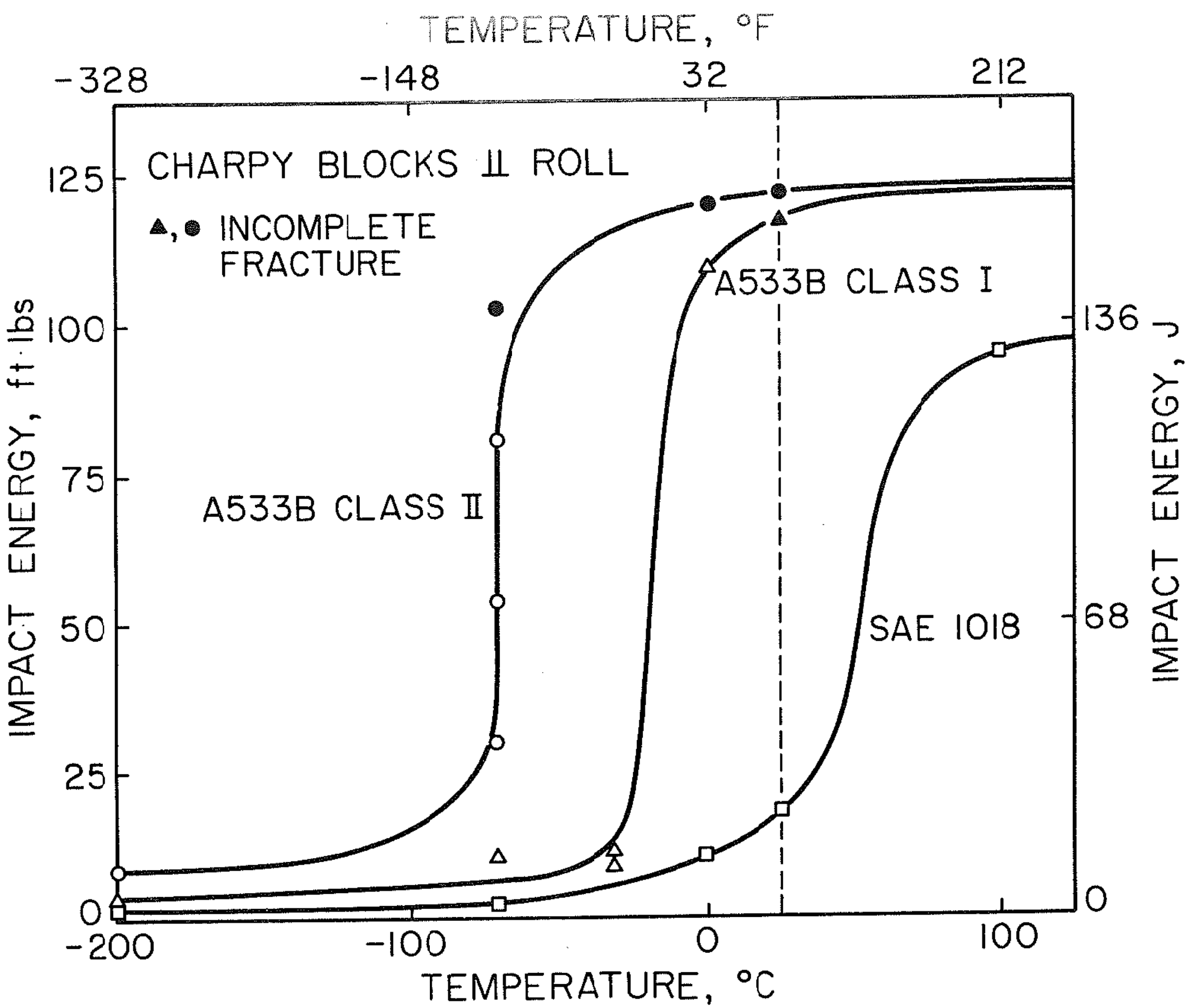

Figure 4.1 Impact Test Results for SAE 1018, A533B Class I & II Steels

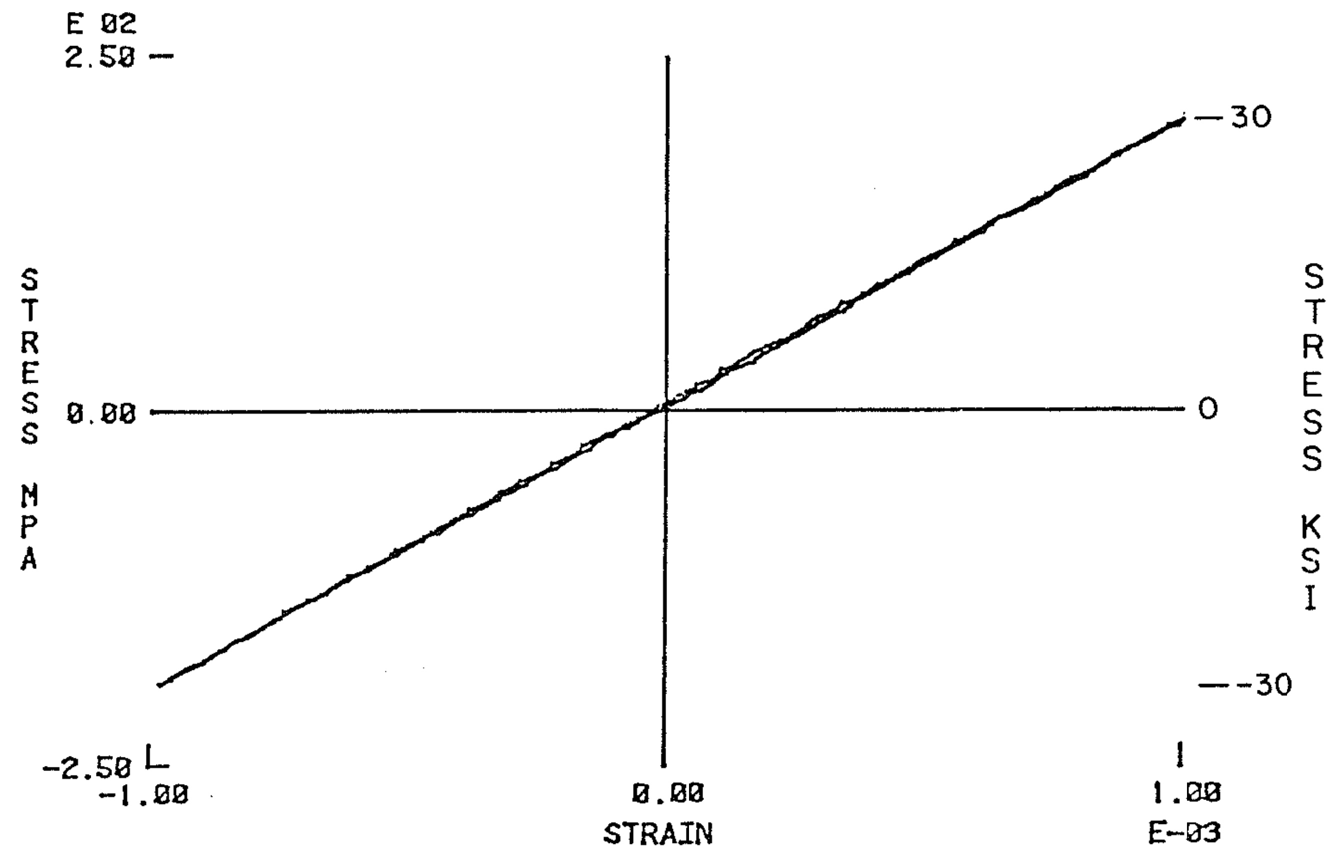

Figure 4.2 Typical stress-strain plot for SAE 1018, A533B Class I & II from 1.0 to 10^6 cycles

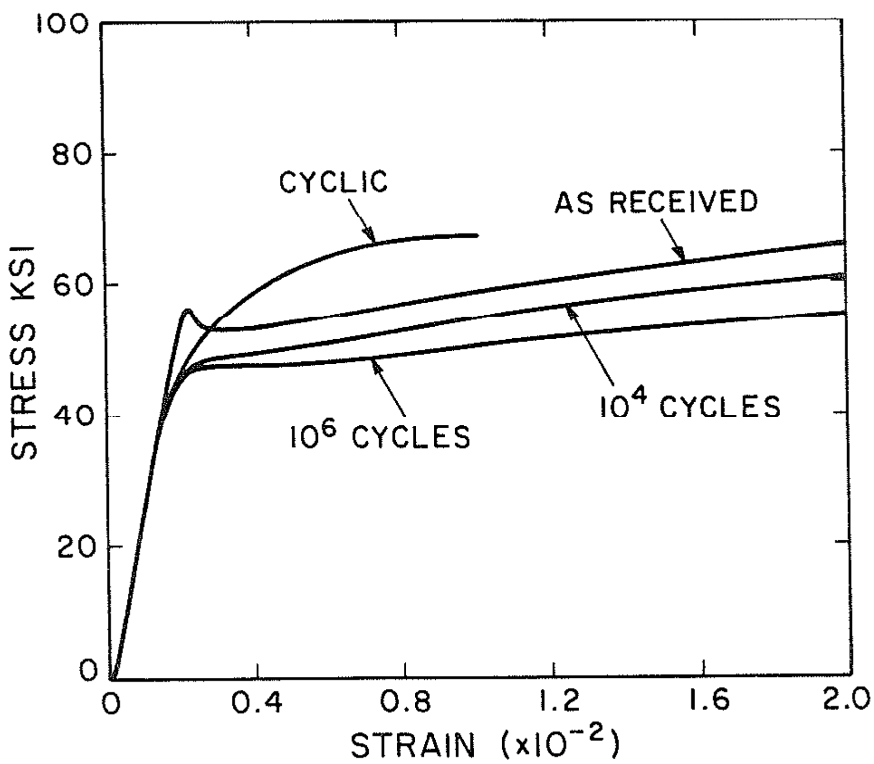

Figure 4.3 Cyclic and Monotonic tensile curves for as-received and pre-fatigued SAE 1018 steel at room temperature

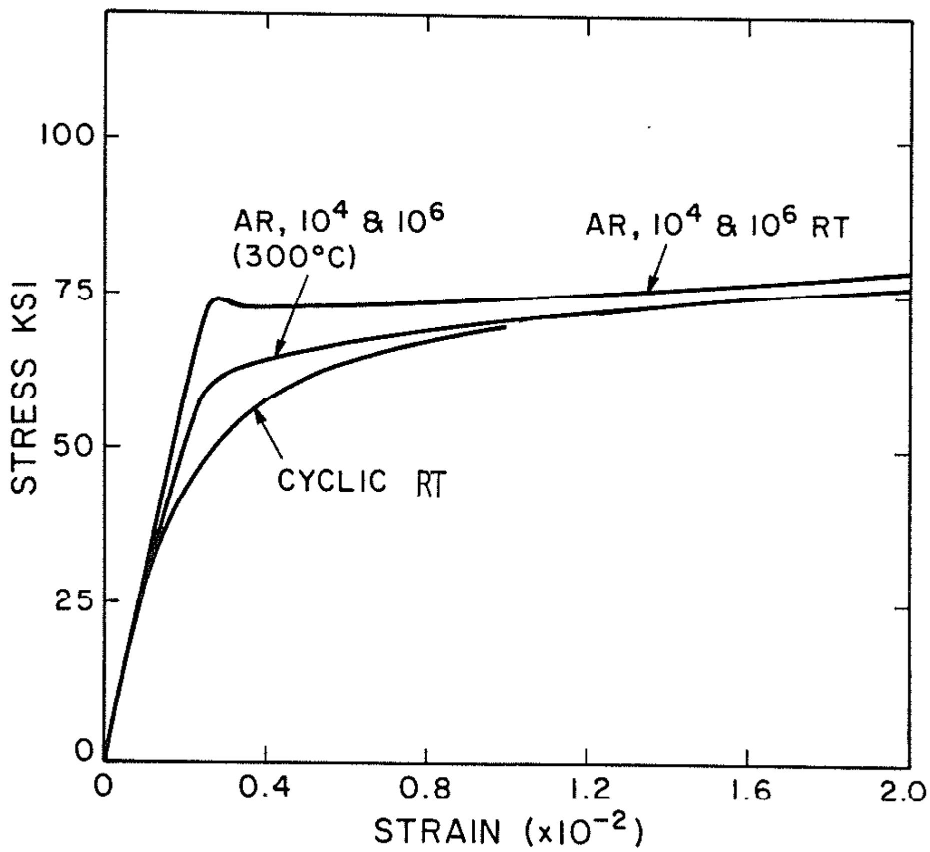

Figure 4.4 Cyclic and Monotonic tensile curves for as-received and pre-fatigued A533B Class I pressure vessel steel at room temperature and 300°C

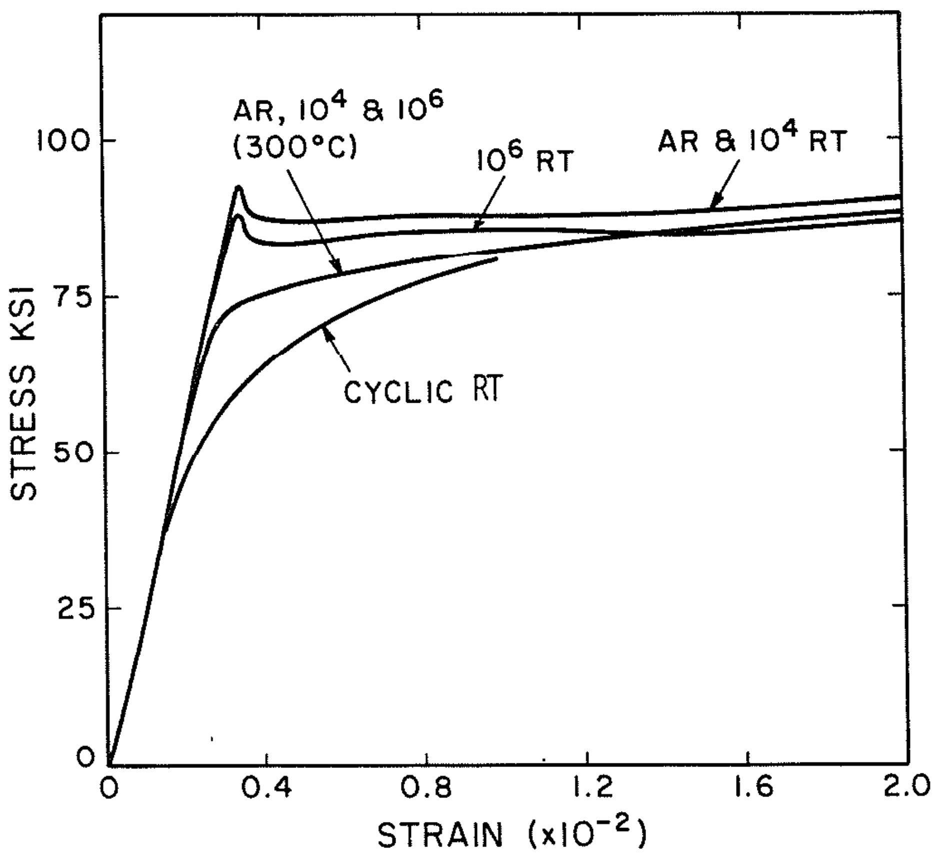

Figure 4.5 Cyclic and Monotonic tensile curves for as-received and pre-fatigued A533B Class II pressure vessel steel at room temperature and 300^{0}C

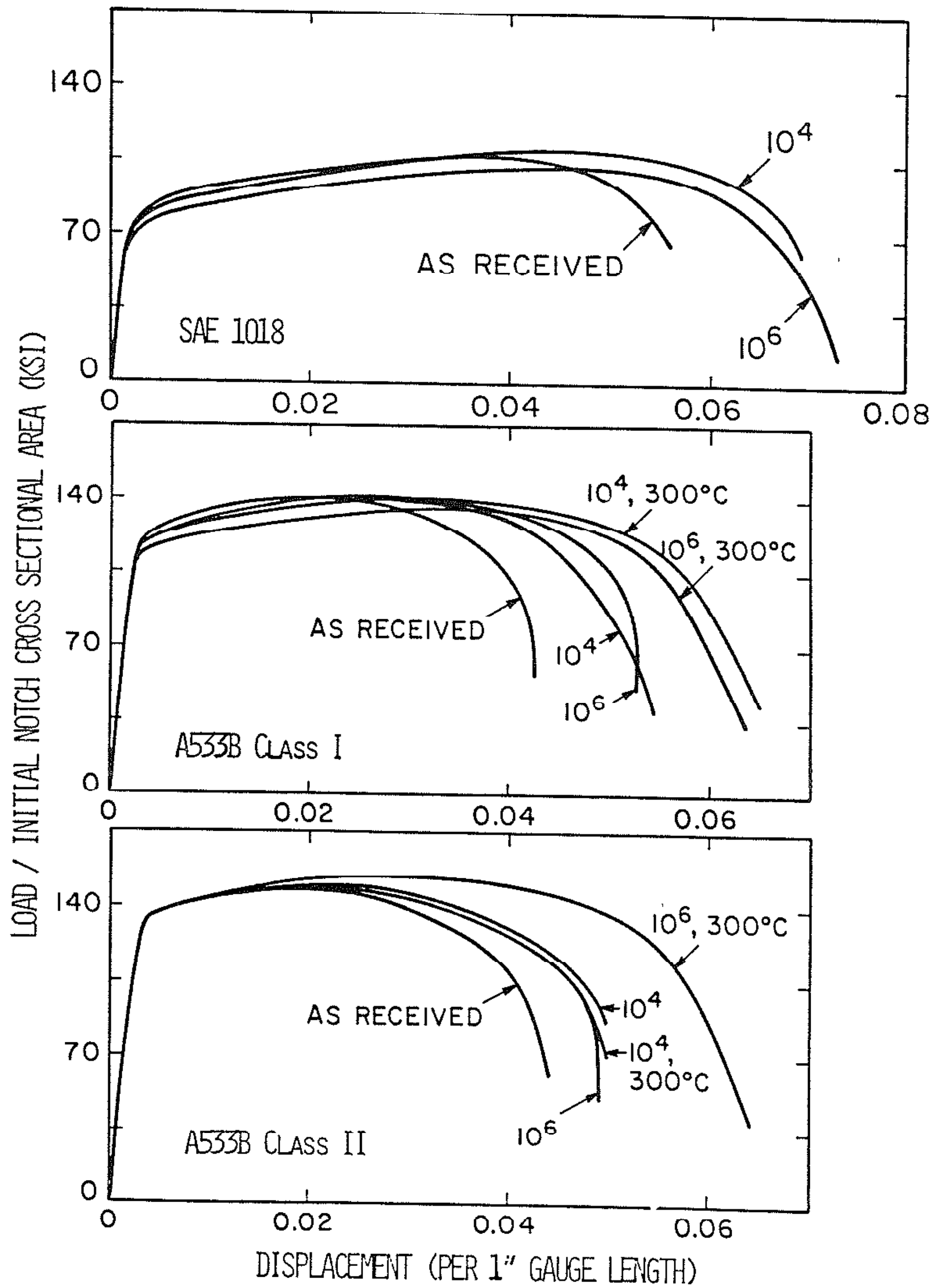

Figure 4.6 Notched Tensile Curves for As-received and Pre-fatigued SAE 1018, A533B Class I, & A533B Class II Steels.

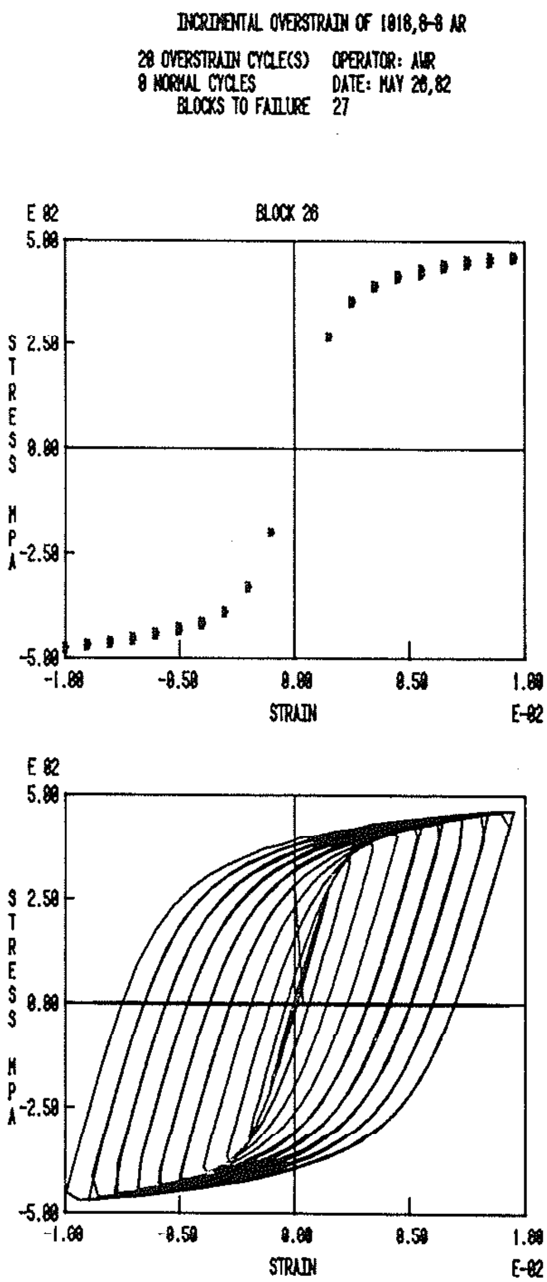

Figure 4.7 Cyclic Stress-Strain Curve for SAE 1018

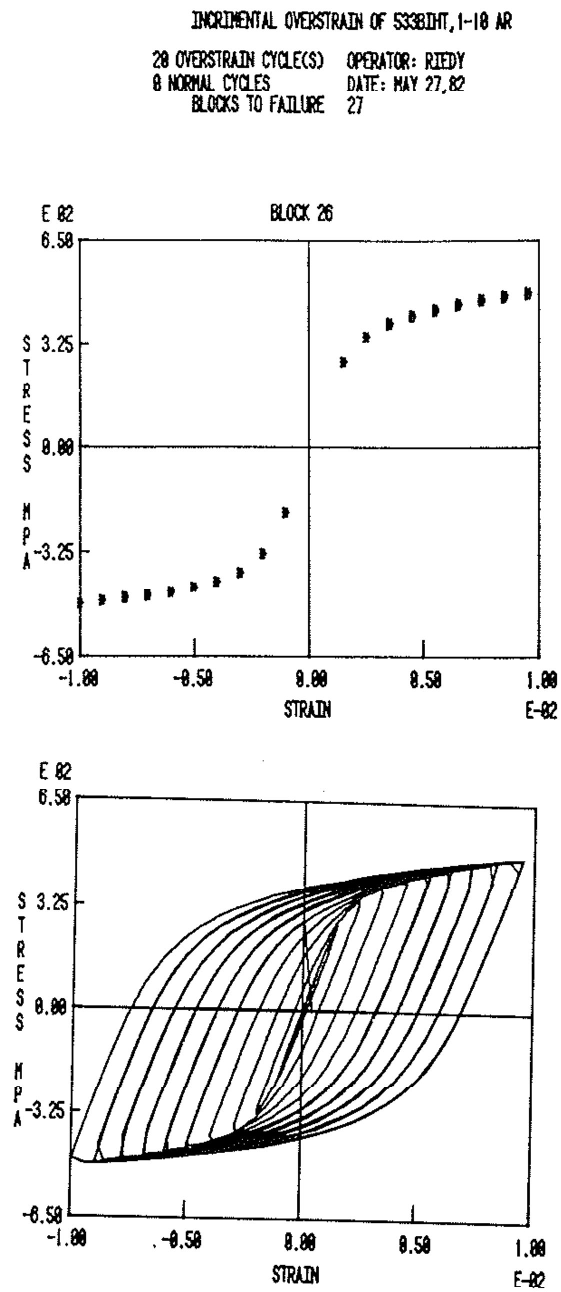

Figure 4.8 Cyclic Stress-Strain Curve for A533B Class I

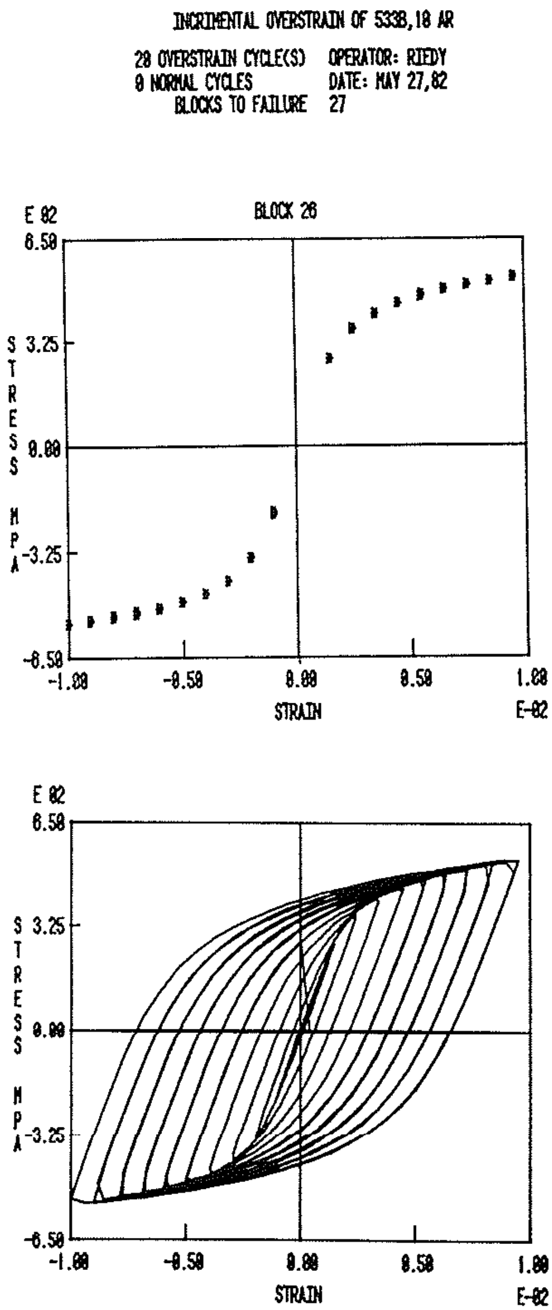

Figure 4.9 Cyclic Stress-Strain Curve for A533B Class II

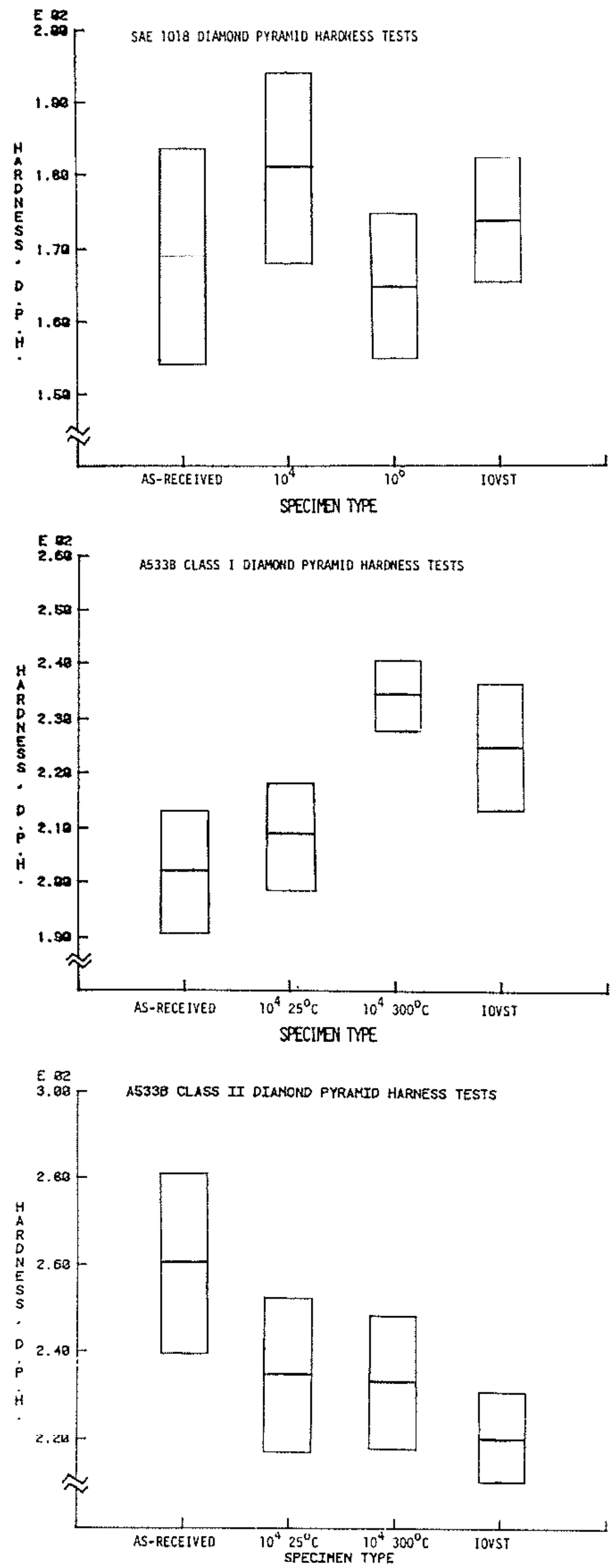

Figure 4.10 Diamond pyramid hardness tests for SAE 1018, A533B Class I, and A533B Class II (Mean values $\pm \sigma$)

SAE 1018

50 μm

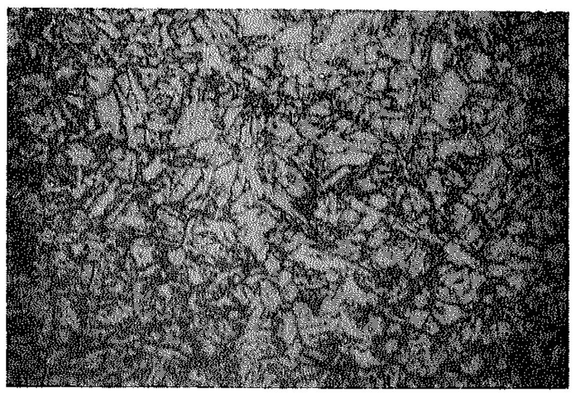

A533B Class I

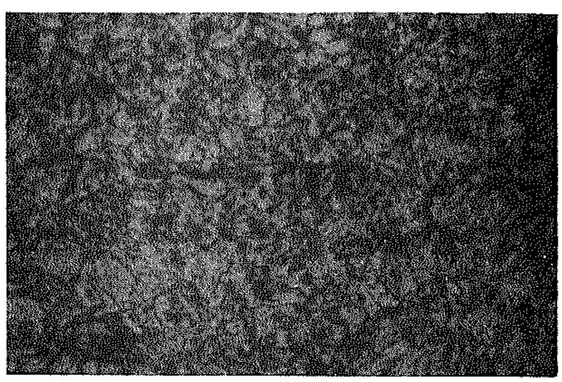

A533B Class II

Figure 4.11 Grain structures of SAE 1018, A533B Class I, & A533B Class II steels (Optical Micrographs)

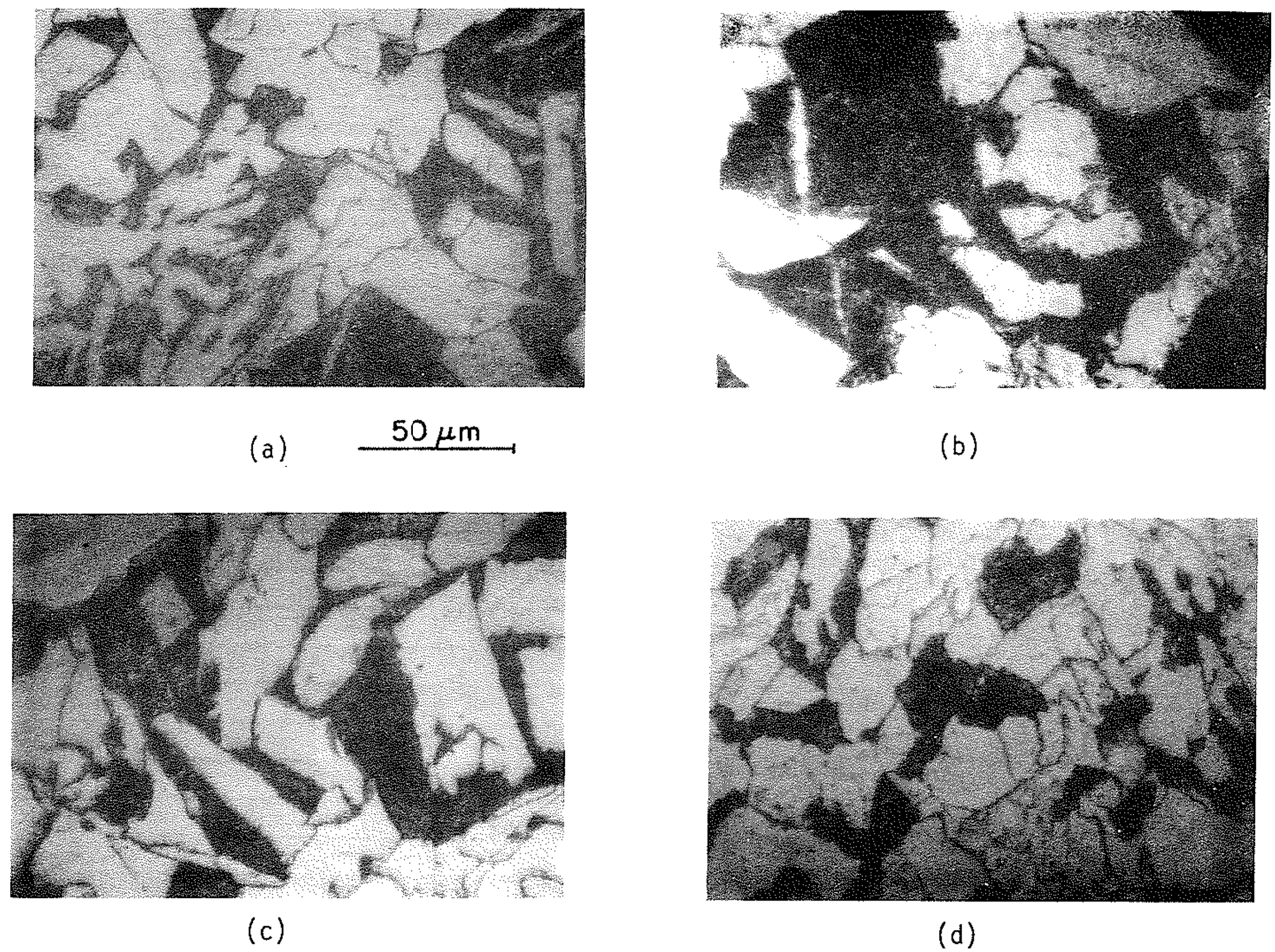

Figure 4.12 Micrographs of SAE 1018: (a) As-received, (b) Fatigued to 10^4 cycles, (c) Fatigued to 10^6 cycles, (d) Incremental Over-strain to 1% (Optical)

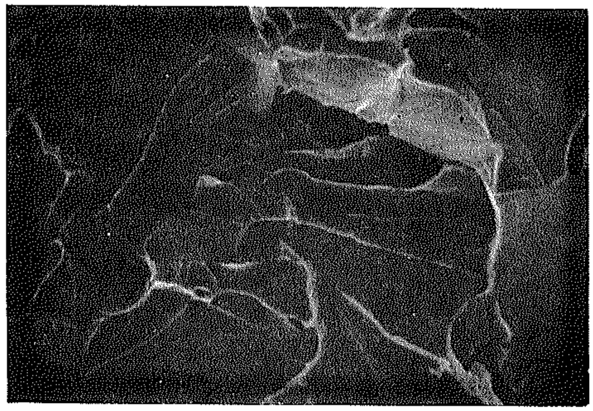

As-received 50 μm

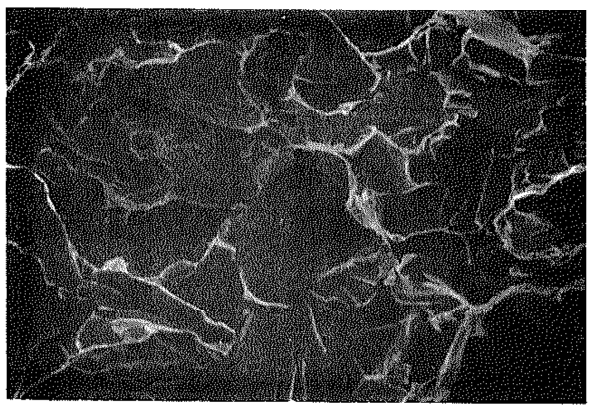

10^4 cycles, 25^oC

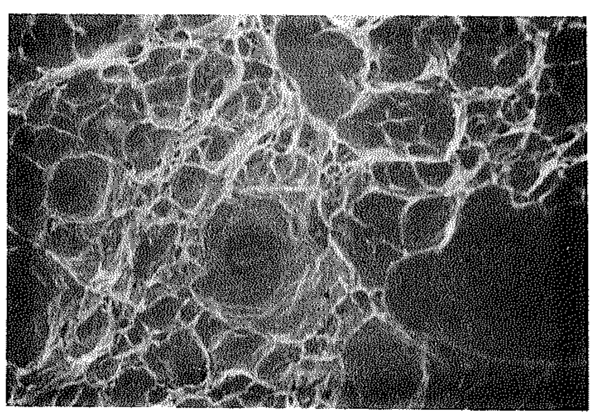

10^6 cycles, 25^oC

Figure 4.13 Scanning Electron Microscope Photographs of SAE 1018 Notch-Tensile Fracture Surfaces

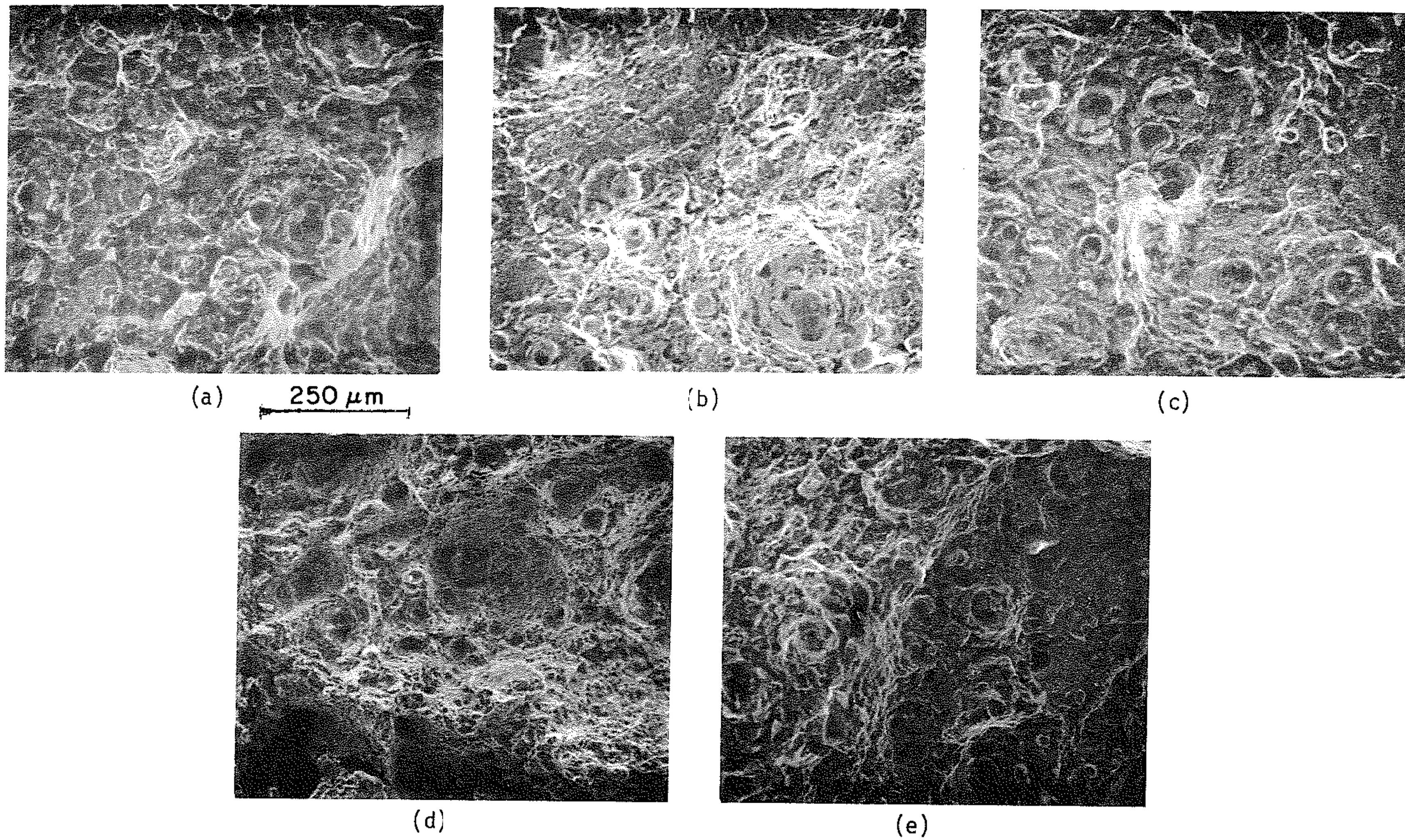

Figure 4.14 Scanning Electron Microscope Photographs of A533B Class I Notch-Tensile Fracture Surfaces: (a) As-received 25°C, (b) 10^4 cycles 25°C, (c) 10^6 cycles 25°C, (d) 10^4 cycles 300°C, (e) 10^6 cycles 300°C.

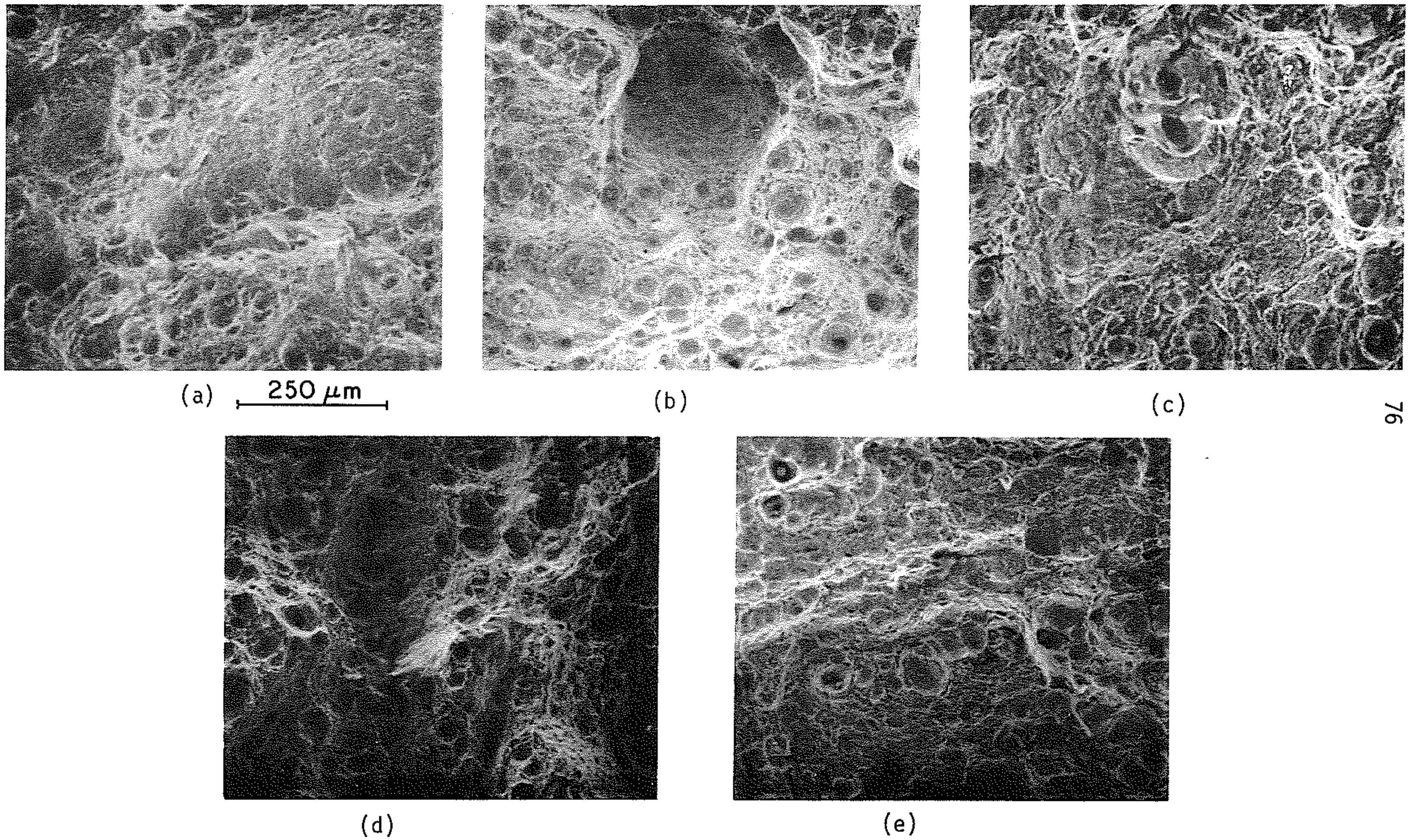

Figure 4.15 Scanning Electron Microscope Photographs of A533B Class II Notch-Tensile Fracture Surfaces: (a) As-received 25°C, (b) 10^4 cycles 25°C, (c) 10^6 cycles 25°C, (d) 10^4 cycles 300°C, (e) 10^6 cycles 300°C.

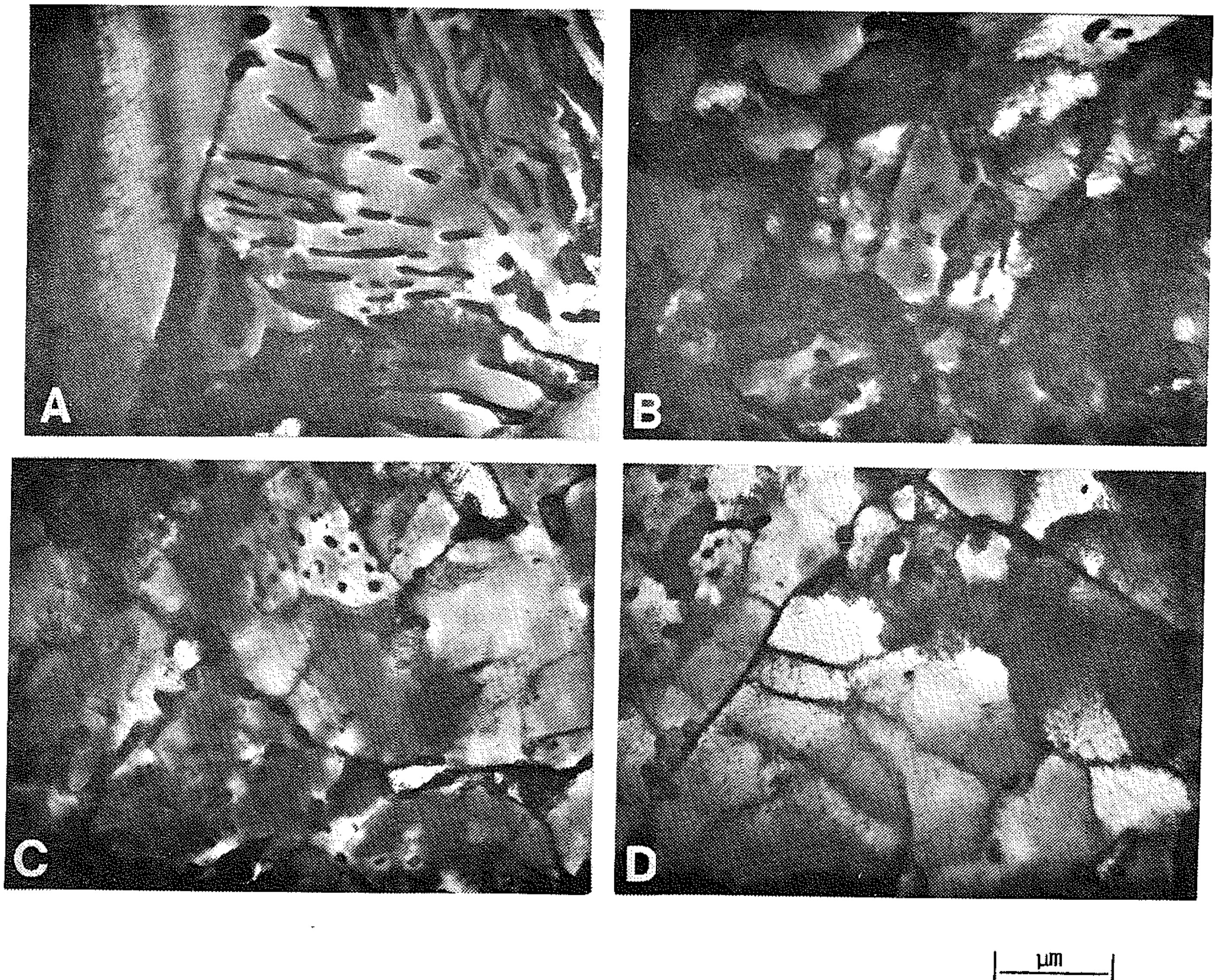

Figure 4.16 Transmission Electron Micrographs of SAE 1018: (A) As-received, (B) Fatigued to 10^4 cycles, (C) Fatigued to 10^6 cycles, (D) Incremental Over-Strain to 1%

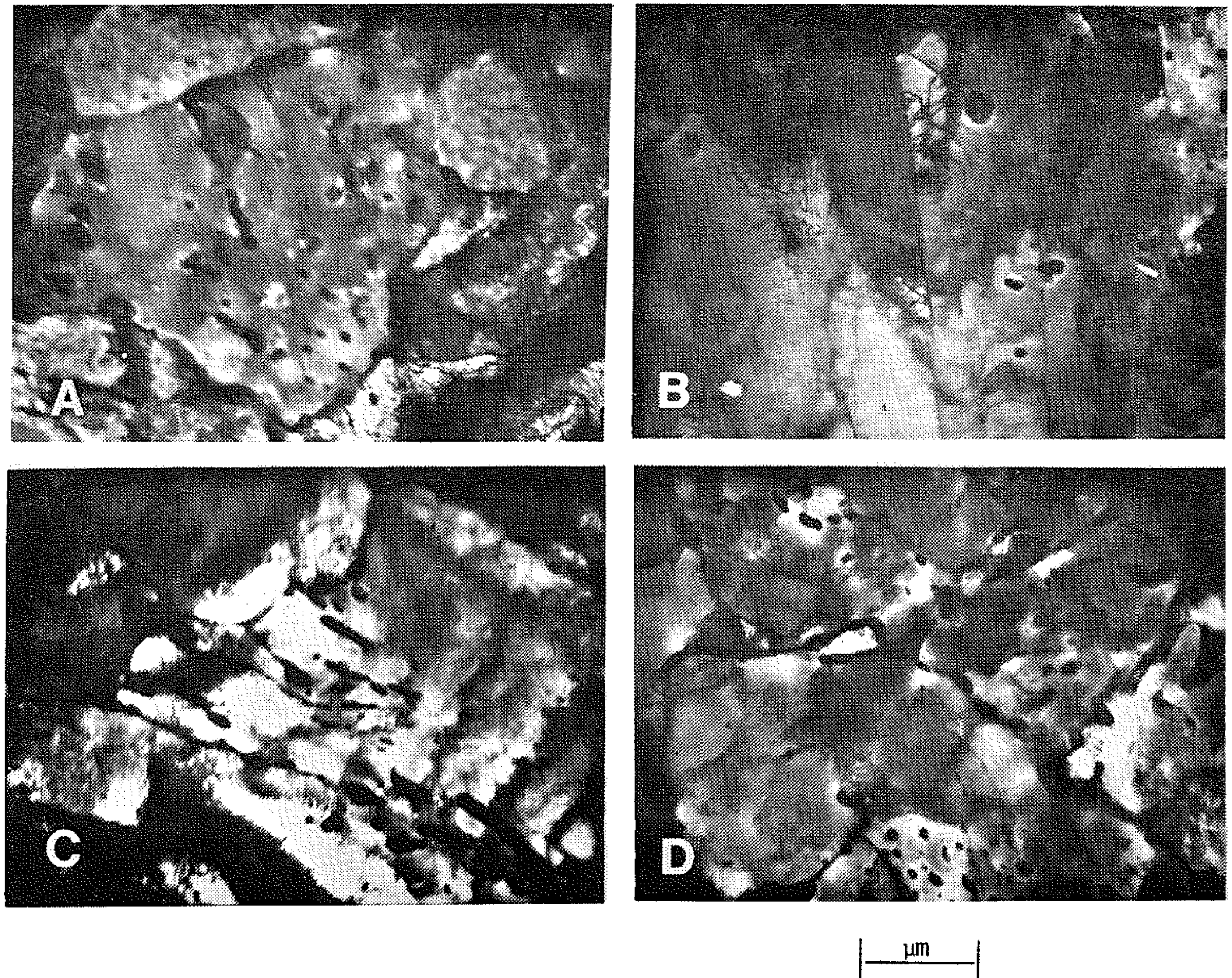

Figure 4.17 Transmission Electron Micrographs of A533B Class I: (A) As-received, (B) Fatigued to 10^4 cycles, 25°C, (C) Fatigued to 10^4 cycles, 300°C, (D) Incremental Over-Strain to 1% at 25°C

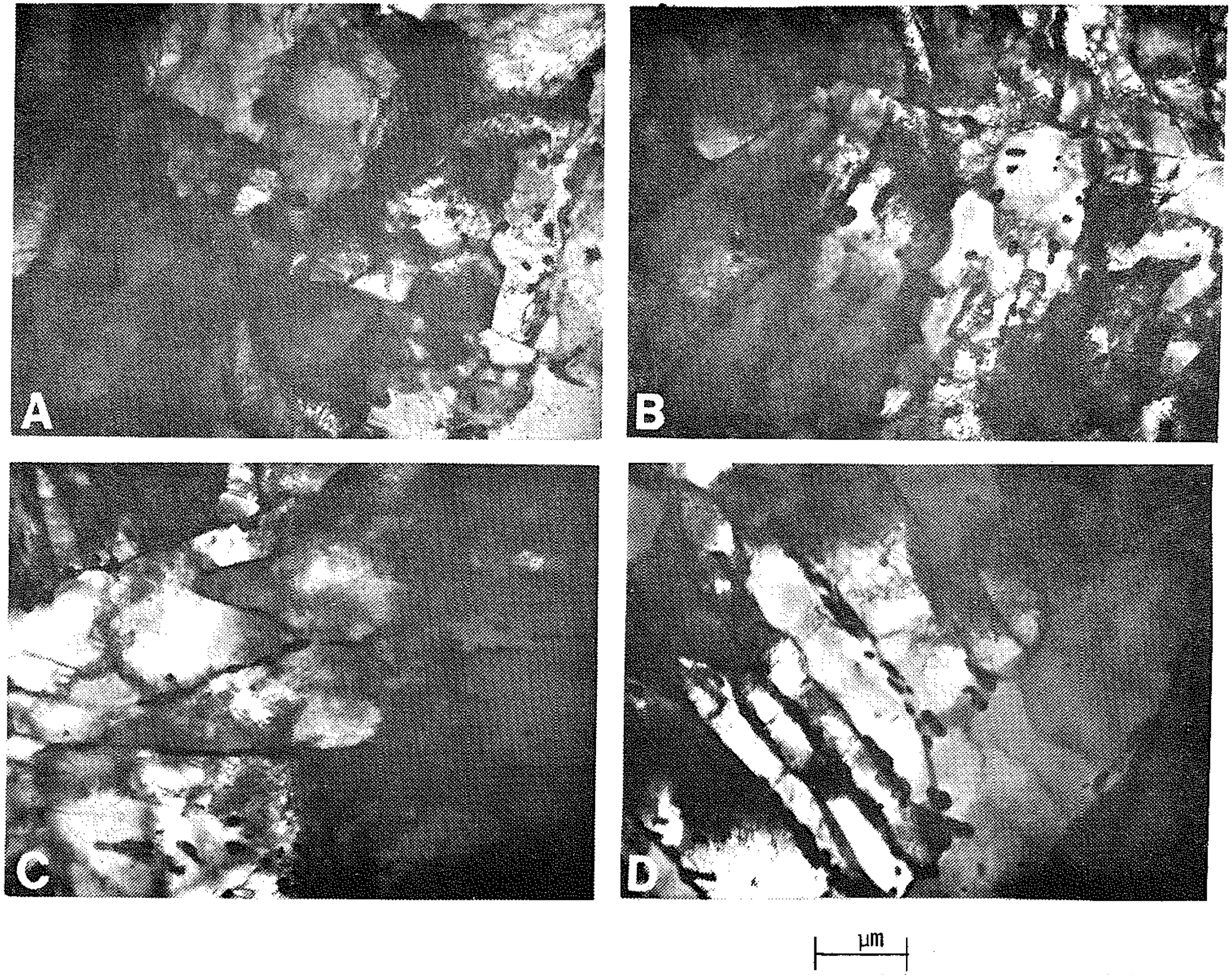

Figure 4.18 Transmission Electron Micrographs of A533B Class II: (A) As-received, (B) Fatigued to 10^4 cycles, 25°C, (C) Fatigued to 10^4 cycles, 300°C, (D) Incremental Overstrain to 1% at 25°C

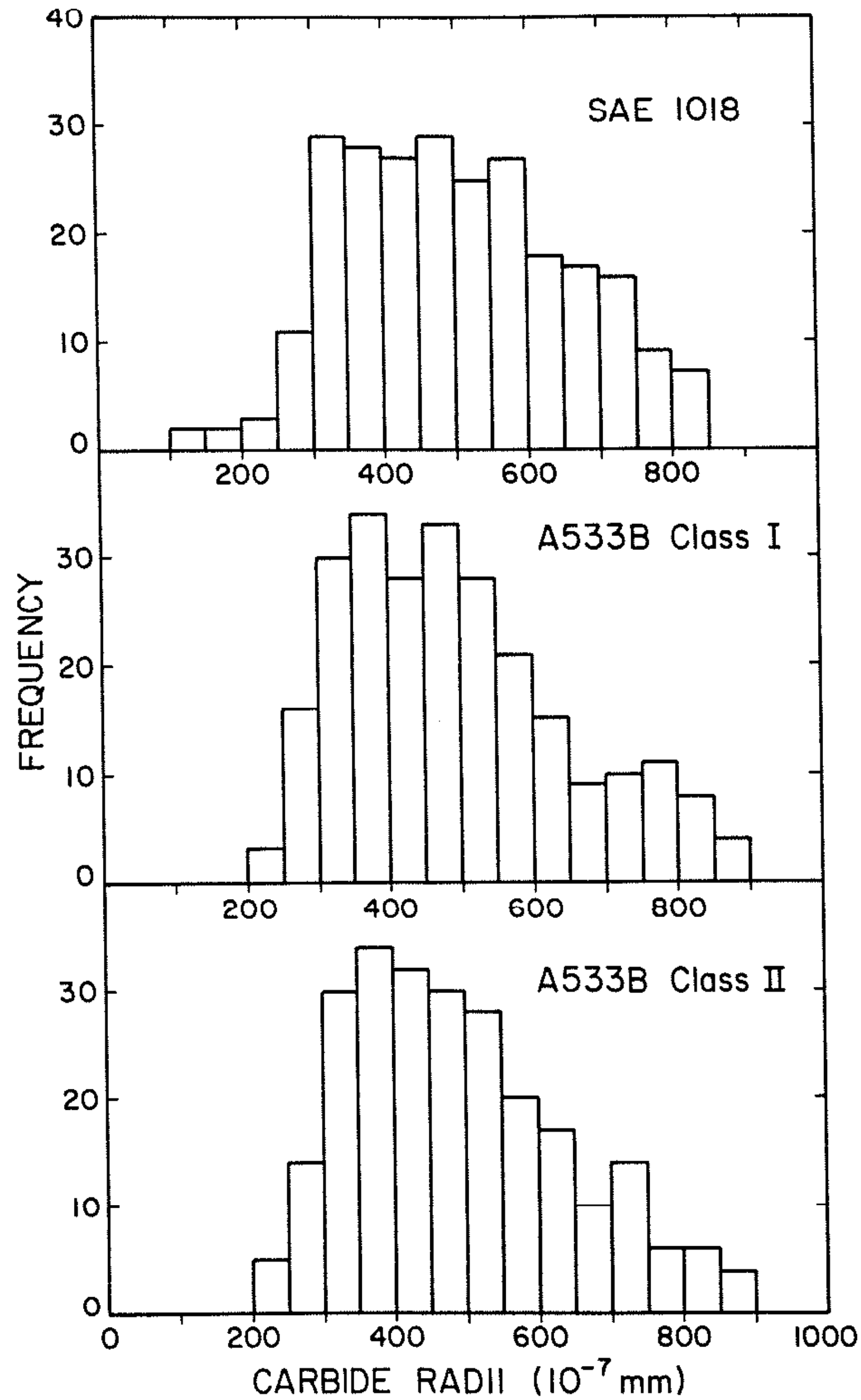

Figure 4.19 Frequency Distribution of Carbide Sizes Observed in TEM Micrographs of SAE 1018, A533B Class I, and A533B Class II

APPENDIX A

```
STRESS   8-NOV-82  MU BASIC/RT-11 V04.00

50 FDUMP \ QUIT
70 FG(1,0)
75 R7=0
100 DIM X(3),A(500),B(20) \ GOSUB 1000
150 BUTN("S", LINE 7500 ) \ BUTN("H", LINE 7000 ) \ BUTN("C", LINE 7700
)
200 IF I1=1 THEN 7000 \ GOSUB 2000
300 GO TO 200
999 REM  ***  INPUT TEST INFORMATION  ***
1000 PRINT "SAMPLE DESCRIPTION:"; \ INPUT S$
1001 PRINT "TEMPERATURE FOR THE TEST:"; \ INPUT H$
1010 PRINT "YOUR INITIALS:"; \ INPUT I$ \ PRINT "THE DATE:"; \ INPUT T$
1029 PRINT "NO. OF CYCLES FOR THE TEST :"; \ INPUT L9
1030 PRINT "STRAIN TRANSDUCER AMP. AT 10 V.:"; \ INPUT A1 \ S1=A1/2047
1040 PRINT "AMPLITUDE (KSI), MEAN (KSI) :"; \ INPUT Q2,R2
1060 PRINT "LOAD TRANSDUCER AMP. AT 10 V. (KIPS):"; \ INPUT A3
1070 PRINT "SPECIMEN DIAMETER (IN):"; \ INPUT D1 \ S2=A3/D1^2*4.28650E-0
3
1071 A2=Q2*((D1/2)^2)*PI
1072 M2=R2*((D1/2)^2)*PI
1075 PRINT "INPUT DATA INTERVAL" \ INPUT M9
1080 M3=INT(2047*(M2+A2)/A3) \ M4=-INT(-2047*(M2-A2)/A3)
1090 PRINT "FREQUENCY FOR THE TEST(HZ):"; \ INPUT F1
1100 F3=.1 \ IF F3>F1 THEN F3=F1
1110 F2=INT(F1*409.5) \ F4=INT(F3*409.5)
1120 T1=INT(50/F3) \ P1=INT(10000/T1/F3) \ P2=INT(10000/T1/F1)
1130 PRINT "PERCENT STRAIN RISE TO DEFINE FAILURE:"; \ INPUT L1
1140 PRINT "NAME OF DATA FILE FOR HYSTERESIS LOOPS:"; \ INPUT D1$
1150 PRINT "NAME OF DATA FILE FOR OTHER INFORMATION:"; \ INPUT D2$
1155 PRINT "DEVICE FOR DATA STORAGE:"; \ INPUT D3$
1158 D4$=D3$+D1$ \ D5$=D3$+D2$
1170 OPEN D4$ FOR OUTPUT AS FILE #3 DOUBLE BUF, FILESIZE 59
1175 FOR I=1 TO 29 \ AOUT(#3,A(1),-1,B5,B6)
1180 B5=B5+2 \ NEXT I
1185 CLOSE #3 \ B5=0
1186 N2=29 \ GO TO 7060
1189 N2=0
1190 PRINT "TYPE <CR> TO START TEST" \ INPUT Q9$
1191 TIME(T1)
1999 REM  ***  MAIN PART OF PROGRAM  ***
2000 X=3 \ X(0)=0 \ X(1)=F4 \ X(2)=M3 \ X(3)=M4 \ A=1
2010 GOSUB 6000 \ IF N<>0 THEN 2030
2020 N=N+1 \ N2=N2+1 \ GO TO 2010
2030 N1=2^N-1 \ X(1)=F2 \ ENABL
2040 IF N<4 THEN  GOSUB 5000 \ GO TO 2090
2050 IF N>4 THEN GOSUB 4000 \ GO TO 2070
2060 GOSUB 3000 \ GO TO 2090
2070 IF N2=29 THEN I1=1 \ I2=1
2080 IF I1=1 THEN DSABL \ RETURN
2090 N2=N2+1 \ IF N<14 THEN N=N+1
2100 DSABL \ RETURN
2999 REM  ***  FINDS AVERAGE OF MAX LOAD FOR CYCLES 17-26 FOR REFERENCE
3000 DACQ(4,B,1,P2) \ FG(1,X,N1,3,4) \ START
3010 IF B<10 THEN 3010
3020 QUIT \ FOR J=1 TO 10 \ B1=B1+B(J)
3030 PRINT B(J); \ NEXT J \ B2=B1*.11 \ B1=B1*(1+L1/100)/10
```

APPENDIX A

Appendix A contains a description of the values which constitute the input to the program STRESS.BAR. Following this is a listing of the program. The STRESS.BAR program was developed to run load controlled fatigue tests in conjunction with a MTS test stand. This program will fatigue a specimen to an inputed number of cycles or to failure, which ever comes first, and it will store hysteresis loop data at 32 + M9 cycles, 32 + 2(M9) cycles and so on (where M9 is the data storeage interval). The following variables must be assigned values for the STRESS.BAR program to be run:

L9 = Number of cycles for the test

A1 = Strain tansducer amplitude at 10 volts

Q2 = Stress amplitude (ksi)

R2 = Mean stress (ksi)

A3 = Load transducer amplitude at 10 volts

D1 = Specimen diameter (inches)

M9 = Data storage interval

F1 = Freqeuncy for the test (Hz)

L1 = Percent strain rise to define failure

D1$ = Name of data file for hysteresis loops

D2$ = Name of data file for other information

D3$ = Device for storage, either DXØ:, DX1:, FIØ:, or FI1:

Data can be sorted on either single or double density 8 inch floppy discs. Data sotred by the STRESS.BAR program can be analyzed with the BILMMX.BØØ or BILHLP.BØØ program.

```
3040 LEFT(1,G1,G2,G3,G4) \ IF G3>0 THEN 3040
3045 PRINT
3050 RETURN
3999 REM  ***  RUNS TEST AFTER CYCLE 32 AND CHECKS FOR FAILURE  ***
4000 IF N2>14 THEN N3=N3+1
4010 DACQ(4,C,1,P2) \ DACQ(4,D,1,P2) \ START
4011 N8=M9
4012 IF N8<=32767 THEN C8=N8 \ N8=0 \ GO TO 4020
4013 N8=N8-32767 \ C8=32767
4020 FG(1,X,C8,3,4)
4030 IF D<=0 THEN 4070
4040 IF C<D2 THEN 4070
4050 IF I3=0 THEN I3=1 \ N4=G1/2
4060 IF C>B1 THEN I1=1 \ LEFT(1,G1,G2,G3,G4) \ GO TO 7000
4070 LEFT(1,G1,G2,G3,G4) \ IF G1>L9*2 THEN 7000 \ IF G3>0 THEN 4030
4080 IF N8<>0 THEN 4012
4090 QUIT \ RETURN
4999 REM  ***  RUNS TEST BEFORE CYCLE 16  ***
5000 FG(1,X,N1,3,4)
5010 LEFT(1,G1,G2,G3,G4) \ IF G3>0 THEN 5010
5020 RETURN
5999 REM  ***  RECORDS LOOP AT EACH CYCLE WHICH IS A POWER OF TWO  ***
6000 Z8=Z8+M9 \ IF N<=5 THEN Z8=2^N2
6005 N5=2*N2*P1 \ PRINT 'RECORDING CYCLE # ',Z8
6010 DACQ(3,A,0,1) \ DACQ(6,A,1,1) \ START \ FG(1,X,1,3,4)
6020 IF A<P1*2 THEN 6020
6025 QUIT
6030 OPEN D4$ AS FILE #3 DOUBLE BUF
6035 AOUT(#3,A(1),-1,B5,B6) \ B5=B5+2
6040 CLOSE #3 \ RETURN
6999 REM  ***  STOPS TEST AT FAILURE AND STORES INFORMATION  ***
7000 QUIT \ X=-1 \ FG(1,0)
7010 FOR L=1 TO 500 \ Z1=SIN(L) \ NEXT L \ MSWFG(1,0)
7020 N2=N2+1
7025 IF I2=1 THEN PRINT 'TEST STOPPED AT',G1/2,'CYCLES' \ GO TO 7040
7030 PRINT S$,' FAILED AT ',G1/2,' CYCLES.'
7040 PRINT 'TEST INFORMATION PLACED IN FILE ',D2$,'.'
7050 PRINT 'HYSTERESIS LOOPS PLACED IN VIRTUAL FILE ',D1$,'.'
7055 PRINT '10% STRAIN RISE OCCURRED AT',N4,' CYCLES.'
7057 A2=(A2/A3)*2047
7060 OPEN D5$ FOR OUTPUT AS FILE #1, FILESIZE 1
7070 PRINT #1,S$ \ PRINT #1,T$ \ PRINT #1,I$ \ PRINT #1,A2
7080 PRINT #1,G1/2 \ PRINT #1,D1$ \ PRINT #1,S1 \ PRINT #1,S2
7085 PRINT #1,N4 \ PRINT #1,N2 \ PRINT #1,P1 \ PRINT #1,M9
7086 PRINT #1,R7 \ CLOSE #1
7087 IF I9=0 THEN I9=1 \ GO TO 1189
7090 DUMP \ FG(1,0) \ STOP
7499 REM  ***  INTERRUPT CHECK ROUTINES  ***
7500 PRINT 'CYCLES RUN:',G1/2,,'MAX LOAD:',C*S2 \ PRINT
7530 RETURN
7700 FGHOLD(1) \ PRINT 'TYPE <BREAK> 'C' TO CONTINUE'
7720 FGRESUME(1) \ RETURN
7999 REM  ***  VOLTMETER ROUTINE  ***
8000 QUIT
8010 FOR I=1 TO 500 \ PRINT  \ PRINT  \ PRINT 'LOAD','STRAIN','STROKE'
8020 FOR J=1 TO 18 \ DACQ(0,Q,0,0) \ DACQ(0,R,1,0) \ DACQ(0,S4,2,0)
8030 PRINT Q,R,S4 \ NEXT J \ NEXT I \ QUIT
```

REFERENCES

1. A.A. Griffith, "The Phenomena of Rupture and Flow in Solids", Philosophical Transactions of the Royal Society of London, Series A, Vol. 221, pp. 163-198, (March 1921).

2. P. Ludwik, "Kohasion Harte and Zahigkeit," Zeitschrift fur Metallkunde. Vol. 14, p. 101, (1922).

3. E. Orowan, "Fundamentals of Brittle Behavior in Metals," Fatigue and Fracture of Metals, Wiley, New York, pp. 139-167, (1952).

4. A.S. Eldin and S.C. Collins, "Fracture and Yield Stress of 1020 Steel at Low Temperatures," Journal of Applied Physics, 22, 1296, (1951).

5. E.T. Wessel, "A Tensile Study of Brittle Behavior of a Rimmed Structural Steel," ASTM Proceedings, Vol. 56, pp. 540-552, (1956).

6. A.H. Cottrell, "Theory of Brittle Fracture in Steel and Similar Metals," Transactions of the Metallurgical Society of AIME, pp. 192-203, (April 1958).

7. J.R. Low, Symposium on Relation of Properties to Microstructure, ASM, p. 163, (1954).

8. E.R. Parker, Brittle Behavior of Engineering Structures, Wiley, New York, (1957).

9. G.T. Hahn, W.S. Owen, B.L. Averbach, and M. Cohn, "Micromechanism of Brittle Fracture in a Low-Carbon Steel," Welding Research Supplement, pp. 367S-376S, (Sept. 1959).

10. C.J. McMahon, Jr. and Morris Cohen, "Initiation of Cleavage in Polycrystalline Iron," Acta Metallurgica, Vol. 13, pp. 591-604, (June 1965).

11. T.C. Lindley, G. Oates, and C.E. Richards, "A Critical Appraisal of Carbide Crackign Mechanisms in Ferride/Carbide Aggregates," Acta Metallurgica, Vol. 18, pp. 1127-1136, (Nov. 1970).

12. J. Man, B. Vlach, and M. Holzmann, "Microstructure and Embrittlement of Low-Carbon Steel," Wissenschaftliche Zeitschrift der Technischen Hochschule Otto von Guericke Magdeburg 15, pp. 463-471, (1971).

13. R.O. Ritchie, J.F. Knott, and J.R. Rice, "On the Relationship Between Critical Tensile Stress and Fracture Toughness in Mild Steel," Journal of the Mecahnics and Physics of Solids, Vol. 21, pp. 395-410, (1973).

14. R.O. Ritchie, W.L. Server, and R.A. Wullaert, "Critical Fracture Stress and Fracutre Strain Models for the Prediction of Lower and Upper Shelf Toughness in Nuclear Pressure Vessel Steels," Metallurgical Transactions A, Vol. 10A, pp. 1557-1570, (Oct. 1979).

15. D.A. Curry and J.F. Knott, "The relationship between fracture toughness and microstructure in the cleavage fracture of mild steel," Metal Science, pp. 1-6, (Jan. 1976).

16. D.A. Curry and J.F. Knott, "Effects of microstructure on cleavage fracture stress in steel," Metal Science, pp. 511-514, (Nov. 1978).

17. D.A. Curry and J.F. Knott, "Effect of microstructure on cleavage fracture toughness of quenched and tempered steels," Metal Science, pp. 341-345, (June 1979).

18. D.A. Curry, "Comparison between two models of cleavage fracture," Metal Scinece, pp. 78-80 (Feb. 1980).

19. J.F. Knott, "Micromechanisms of fibrous crack extension in engineering alloys," Metal Science, pp. 327-336, (Aug.-Sept. 1980).

20. J.F. Knott, "Micromechanisms of fibrous crack extension in engineering alloys," Metal Science, pp. 327-336, (Aug.-Sept. 1980).

21. D.A. Curry, "Influence of hydrostatic tension on cleavage fracture of bainitic pressure vessel steel," Metal Science, Vol. 16, pp. 435-440, (Sept. 1982).

22. N.H. Polakowski and A. Palchoudhuri, "Softening of Certain Cold-Worked Metals Under the Action of Fatigue Loads," Proceedings of the 57th Annual Meeting of ASTM, pp. 701-716, (June 13-18, 1954).

23. H. Abdel-Raouf and A. Plumtree, "On the Steady state Cyclic Deformation of Iron, "Metallurgical Transactions, Vol. 2, pp. 1251-1254, (April 1971).

24. G.M. Sinclair, "An Investigation of the Coaxing Effect in Fatigue of Metals," Proceedings of ASTM, Vol. 52, pp. 743-751, (1952).

25. J.B. Krommers, "Effect of Understressing and Overstressing in Fatigue," Proceedings: Society of Experimental Stress Analysis, Vol. 3, No. 2, pp. 137-141, (1946).

26. B. Mintz and D.V. Wilson, "Strain Ageing During the Fatigue of Carbon Steels," Acta Metallurgica, Vol. 18, pp. 947-956, (Sept. 1965).

27. D.V. Wilson and J.K. Tromas, "Effects of Stain Ageing on Fatigue Damage in Low-Carbon Steel," Acta Metallurgica, Vol. 18, pp. 1197-1208, (Nov. 1970).

28. C.C. Li and W.C. Leslie, "Effects of Dynamic Strain Aging on the Subsequent Mechanical Properties of Carbon Steels," Metallurgical Transaction A, Vol. 9A, pp. 1765-1775, (Dec. 1978).

29. Iain LeMay, Principles of Mechanical Metallurgy, Elsevier North Holland, Inc., New York, pp. 128-129, (1981).

30. J.M. Steichen and J.A. Williams, "Effect of Strain rate and Temperature on the Tensile Properties of Irradiated ASTM A533-B Steel," Journal of Nuclear Materials, Vol. 57, pp. 303-311, (1975).

31. J. Holden, "The Hardening and Embrittlement of Mild Steel by Cyclic Stressing at the Fatigue Limit," Acta Metallurgica, Vol. 7, pp. 380-388, (June 1959).

32. M. Klesnil and P. Lukas, "Fatigue Softening and Hardening of Annealed Low-carbon Steel," Journal of the Iron & Steel Institute, Vol. 205, p. 746-769, (July 1967).

33. A. Abel and H. Muir, "The Effect of Cyclic Loading on Subsequent Yielding," Acta Metallurgica, Vol. 21, pp. 93-97, (Feb. 1973).

34. A.H. Cottrell and B.A. Bilby, "Dislocation Theory of Yielding and Strain Ageing of Iron," Proceedings of the Physical Society, Vol. 62, pp. 49-62, (1949).

35. A.H. Cottrell, The Mechanical Properties of Matter, John Wiley, New York, p. 282 (1964).

36. A.H. Cottrell, An Introduction to Metallurgy, Edward Arnold Ltd., London, (1967).

37. W.G. Johnston and J.J. Gilman, "Dislocation Velocities, Dislocation Densities, and Plastic Flow in Lithium Fluoride Crystals," Journal of Applied Physics, Vol. 30, pp. 129-144, (1959).

38. G.T. Hahn, "A Model For Yielding With Special Reference To The Yield-Point Phenomena of Iron and Related BCC Metals," Acta Metallurgica, Vol. 20, pp. 727-738, (Aug. 1962).

39. A. Abel and H. Muir, "The Bauschinger Effect and Discontinuous Yielding," Philosophical Magazine, Vol. 26, pp. 489-504, (1972).

40. S. Mader, A. Seeger, and C. Leitz, "Work Hardening and Dislocation Arrangement of fcc Single Crystal. I. Plastic Deformation and Slip Line Studies of Nickel Single Crystals," Journal of Applied Physics, Vol. 34, No. 11, pp. 3368-3375, (Nov. 1963).

41. E. Orowan, "Causes and Effects of Internal Stresses," Internal Stresses and Fatigue in Metals, General Motors Symposium, Elsevier Publishing Co., New York, (1959).

42. J.G. Kaufman, G.T. Sha, R.F. Kohm, and R.J. Bucci, "Notch-Yield Ratio as a Quality Control Index for Plain Strain Fracture Toughness," Cracks and Fracture, ASTM-STP 601, ASTM, pp. 169-190, (1976).

43. V.S. Ivanova, L.G. Orlov, V.F. Terent'Yev, and V.G. Poyda, "Features of the Development of Dislocation Structure in a Low-carbon Steel Under Static and Periodic Alternating Load," Physics of Metals and Metallography, Vol. 33, No. 3, pp. 167-172, (1972).

44. M. Klesnil and P. Lukas, "Dislocation Arrangement in the Surface Layer of -iron Grains during Cyclic Loading," Journal of the Iron and Steel Institute, pp. 1043-1048, (Oct. 1965).

45. J.D. Groom and J.F. Knott, "Cleavage Fracture in Prestrained Mild Steel," Metal Science, Vol. 9, pp. 390-400, (1975).

46. G. Oates, "Effect of Temperature and Strain Rate on Cleavage Fracture in a Mild Steel and a Low-carbon Manganese Steel," Journal of the Iron and Steel Institute, Vol. 207, pp. 353-357, (March 1969).

47. P. Brozzo, G. Buzzichelli, A. Mascanzoni, and M. Mirabile, "Microstructure and cleavage resistance of low-carbon bainitic steels," Metal Science, Vol. 11, pp. 123-129, (April 1977).

48. E. Smith, "The nucleation and growth of cleavage microcracks in mild steel," Physical Basis of Yield and Fracture: Conference Proceedings, Institute of Physics and Physical Society, Oxford, pp. 36-46, (Sept. 1966).

49. J.R. Griffiths and D.R.J. Owen, "An Elastic-Plastic Stress Analysis for a Notched Bar in Plane Strain Bending," Journal of the Mechanics and Physics of Solids, Vol. 19, pp. 419-431, (1971).